Fakultät für Physik und Astronomie

Ruprecht-Karls-Universität Heidelberg

Masterarbeit

Im Studiengang Physik

vorgelegt von

Farshad Shobeiry

geboren in Teheran (Iran)

2017

Time-Resolved Study of Double-Ionization of Atoms

Die Masterarbeit wurde von Farshad Shobeiry

ausgeführt am

Max-Planck-Institut für Kernphysik

unter der Betreuung von

Priv.-Doz. Robert Moshammer

Zeitaufgelöste Untersuchung von Einzelphoton – Doppelionisation in Atomen:

Diese Arbeit ist Teil eines Projekts zur zeitaufgelösten Untersuchung der Mehrteilchendynamik und – korrelation von Ein-Photon – Doppelionisationsprozessen in Atomen. Die Komibation eines XUV-IR Pump-Probe Experiments mit einem Reaktionsmikroskop (ReMi) ermöglicht die vollständige Messung der Reaktionskinematik auf Attosekundenzeitskala: Ein Attosekundenpulszug erzeugt durch hohe harmonische (HHG) doppelionisiert das Atom (Pump) und der Überlapp mit einem zeitlich verzögerbaren IR-Puls (Probe) führt zu Interferenz zwischen den ionisierten Elektronenwellenpaketen. Diese Interferenz wurde als Zeitreferenz und zur Charakterisierung der Attosekundenpulszüge verwendet (RABBIT). Daraufhin wurden die gemessenen Impulse der ionisierten Elektronen auf Korrelation und Abhängigkeit vom Pump-Probe-Delay untersucht.

Time-Resolved Study of Single-photon Double-Ionization of Atoms:

This work is a part of an ongoing project of the time-resolved investigation of the electron-electron correlation in single-photon double-ionization of atoms. The combination of an attosecond-pump-probe set-up and coincidence measurement powered by a reaction microscope (ReMi) is used which provides us with the full kinematic information on attosecond time scale. High harmonic generation is used to produce an attosecond pulse train as a pump which is temporally and spatially overlapped with the fundamental IR field serving as the probe pulse. By introducing a delay between pump and probe pulses, an interference between photo-electron wave packets is created which serves as an reference to characterize the attosecond pulse train. Finally, the time-resolved study in double-ionization in 2- and 3-particle coincidences is performed.

Contents

1 Introduction

One single photon from a today's table-top laser system can easily deposit enough energy in atoms so that two electrons are freed into the continuum. Single-photon double-ionization (SPDI) can be expressed by

$$\gamma + A \rightarrow A^{2+} + e^- + e^-. \tag{1.1}$$

The explanation of the dynamics of the above simple-looking interaction has puzzled the atomic physics community up to now. Knowing that the light can only couple to one single electron is the clear manifestation of the electron-electron correlation in SPDI. This phenomenon is the key to a better understanding of the dynamics of few-body systems. Moreover, the electron correlation is a major contributing factor to the evolution of the macroscopic world. It is the responsible phenomenon at the heart of chemical reactions. There is also a plethora of instances in which the correlation between electrons plays an important role, e.g. superconductivity [1].

As far as the theory is concerned, the electron correlation has proven to be a challenging topic because it leads to an atomic potential for each electron which depends on the coordinates of other electrons, and as a result, the potential is not an effective central potential [2].

On the experimental side, studying SPDI is difficult because all the charged particles during the double-ionization have to be simultaneously detected. Fortunately, with the help of the reaction microscope (ReMi) one can create the full image of the momentum vectors of all charged particles as a result of its 4π solid angle acceptance.

With full kinematic information of the system, the next step is to investigate its dynamics. In other words, any evolution or change in the system should be studied as a function of time. This is another difficulty because of the very small time scale of the atomic dynamics which requires high precision and stability during an experiment.

1.1 Time-scale of Atomic Dynamics

To get an idea about the atomic time scale, one can consider the wave packet of a particle in a superposition of its ground and the first excited state with energies E_0 and E_1 respectively. The solution to the Schrödinger equation shows an oscillatory motion with a period of $T = \frac{2\pi\hbar}{E_1 - E_0}$ suggesting that the molecular vibration is on the femtosecond time scale, and individual electron motions range from tens of femtoseconds to less than an attosecond [3]. In figure 1.1, the time scale of different systems is given for different energy ranges.

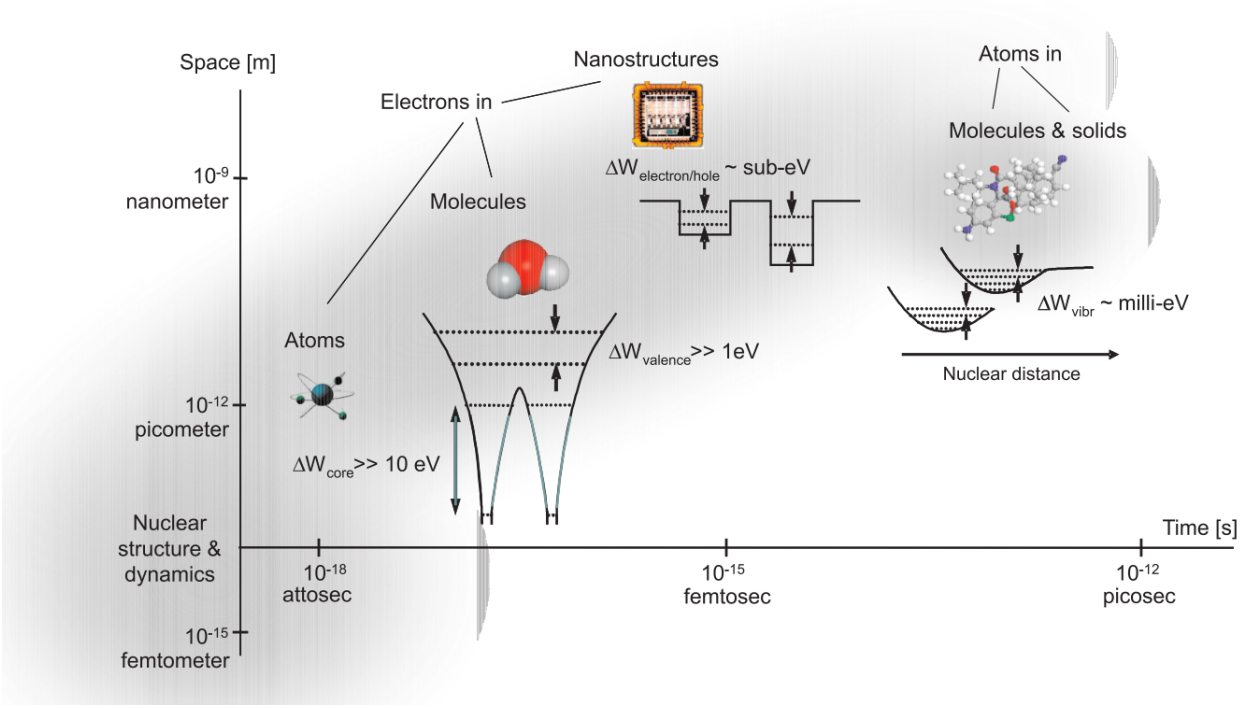

Figure 1.1: The time and length scale on the molecular and atomic levels. Figure taken from [3]

1.2 Aim and Outline of This Thesis

The aim of this thesis is to study the dynamics of the electron-electron correlation during the single-photon double-ionization of atoms. In the first chapter the ultra-short pulses are defined and their characteristics are addressed. Then, the atom field interactions including single-photon single- and double-ionization as well as strong-field ionization are described. In chapter 4, the high harmonic generation (HHG) and its properties are presented. Moreover, the experimental setup is explained briefly in chapter 5 and 6. Finally, the last chapter presents the experimental data on argon and krypton as the gas target in the ReMi.

2 Ultra-short Pulses and Their Propagation

Since the introduction of the laser, in 1960, the pulse duration has gone from a couple of microseconds to a couple of femtoseconds (figure 2.1). Reaching high intensities in laser communities motivated scientists to aim for shorter pulses so as to improve the peak intensities. The transition from the femtosecond time-scale to attosecond has become a reality with the advent of high harmonic generation (HHG). Nowadays, table-top laser systems can deliver reliable few-cycle pulses in the range of sub 10-femtoseconds. This chapter explains the origin of ultra-short pulses, first by introducing a Gaussian beam because most laser cavities produce beams with a Gaussian profile which is the solution to the Maxwell equations. Then a Gaussian pulse, its characteristics, and its propagation in different mediums are explained.

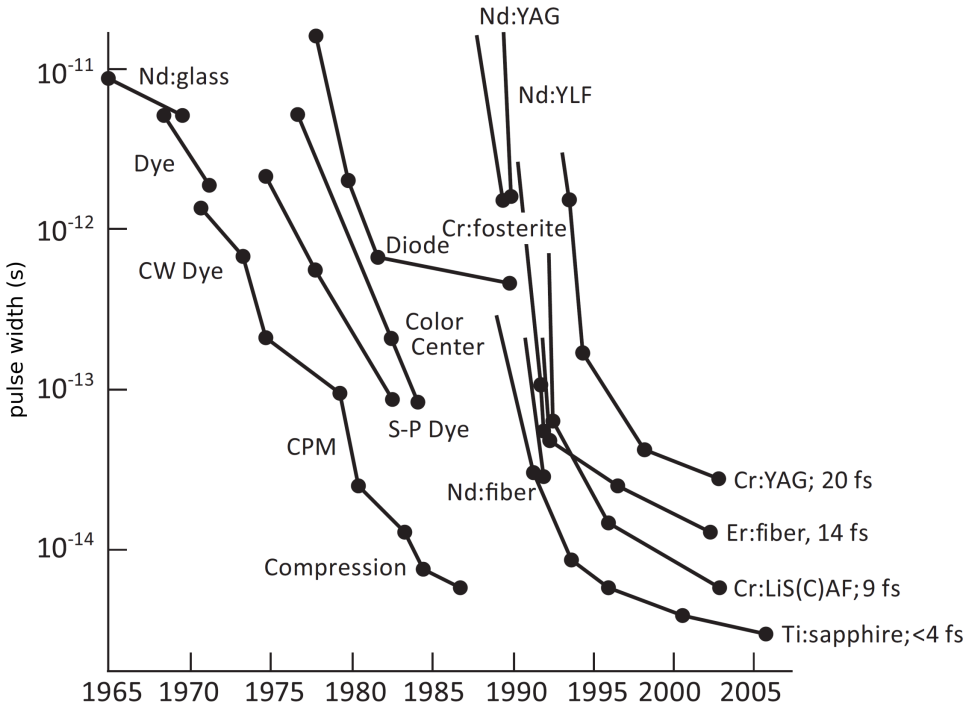

Figure 2.1: The laser timeline. The vertical axis represents the pulse duration produced with different techniques mentioned in the plot. Figure taken from [4]

2.1 Wave Picture of Electromagnetism

Variations of the electric or the magnetic field in one point in space results in the propagation of an electromagnetic wave, which, in a classical picture, is explained by Maxwell's equations:

$$\nabla.\boldsymbol{D} \equiv \nabla.(\epsilon_0\boldsymbol{E} + 4\pi\epsilon_0\boldsymbol{P}) = \rho, \qquad \textit{Gauss's law}$$

$$\nabla.\boldsymbol{B} = 0, \qquad \textit{Absence of free magnetic poles}$$

$$\nabla \times \boldsymbol{E} = -\frac{\partial \boldsymbol{B}}{\partial t}, \qquad \textit{Faraday's law}$$

$$\nabla \times \boldsymbol{H} = (\boldsymbol{J} + \frac{\partial \boldsymbol{D}}{\partial t}), \qquad \textit{Ampere's law with Maxwell's correction } [1]$$

where $\boldsymbol{E}$ is the electric field, $\boldsymbol{P}$ is the polarization of the medium, $\boldsymbol{B}$ is the magnetic induction, ρ is the charge density, ϵ_0 is the electric permittivity of the vacuum, $\boldsymbol{D}$ is the electric displacement, and $\boldsymbol{J}$ is the current density. Contributing factors to the electric displacement vector $\boldsymbol{D}$ and magnetic field $\boldsymbol{H}$ are given by

$$\boldsymbol{D} = \epsilon_0\boldsymbol{E} + (\boldsymbol{P} - \sum \frac{\partial \boldsymbol{Q}}{\partial \chi} + \dots),$$

$$\boldsymbol{H} = \frac{1}{\mu_0}\boldsymbol{B} - (\boldsymbol{M} + \dots), \tag{2.1}$$

the quantities $\boldsymbol{P}, \boldsymbol{M}, \boldsymbol{Q}$ and higher order objects represent the microscopically averaged electric dipole, magnetic dipole, and electric quadrupole of the material medium in the presence of applied fields. The wave equation can be derived by applying $\nabla \times (\nabla \times \boldsymbol{A}) = \nabla(\nabla.\boldsymbol{A}) - \nabla^2\boldsymbol{A}$ to the last two Maxwell's equations. With the assumption of the propagation in vacuum which is free of charge and current [2], one

[1] For detailed explanations refer to [5]

[2] propagation in the free space or vacuum would lead to the following assumptions:

1. Uniformity: μ and ϵ are constant everywhere
2. non-conductivity: $\sigma = 0$ therefore $\boldsymbol{J}$ is zero
3. charge free: $\rho = 0$
4. non-dispersive: both μ and ϵ are not a function of the wavelength, i.e., not a function of time

can get:

$$\begin{aligned}\nabla \times (\nabla \times \boldsymbol{E}) &= \nabla \times (-\frac{\partial \boldsymbol{B}}{\partial t}) \\ &= -\frac{\partial}{\partial t}(\nabla \times \boldsymbol{B}) \\ &= -\epsilon_0 \mu_0 \frac{\partial^2 \boldsymbol{E}}{\partial t^2}.\end{aligned} \tag{2.2}$$

Rewriting the right side of the triple product with $\boldsymbol{J} = 0$ and $\nabla.\boldsymbol{E} = 0$, one obtains

$$\nabla^2 \boldsymbol{E} = \epsilon_0 \mu_0 \frac{\partial^2 \boldsymbol{E}}{\partial t^2}. \tag{2.3}$$

Defining the speed of light $c = \frac{1}{\sqrt{\epsilon_0 \mu_0}}$, and the refractive index of a homogeneous dielectric $n = \sqrt{\epsilon \mu}$, the equation 2.3 can be written in the form:

$$\nabla^2 \boldsymbol{E} - \frac{n^2}{c^2} \frac{\partial^2 \boldsymbol{E}}{\partial t^2} = 0. \tag{2.4}$$

Since both $\boldsymbol{E}$ and $\boldsymbol{B}$ are symmetric in homogeneous dielectrics, the same equation is valid for the magnetic field:

$$\nabla^2 \boldsymbol{B} - \frac{n^2}{c^2} \frac{\partial^2 \boldsymbol{B}}{\partial t^2} = 0. \tag{2.5}$$

In order to solve the above equations, one can assume a plane wave travelling in the z direction ($e^{ikz - i\omega t}$) as a possible solution, the following relationship between the wavenumber k and the frequency ω will establish

$$k = \sqrt{\mu \epsilon}\omega. \tag{2.6}$$

2.1.1 Gaussian beam

With the use of the paraxial approximation, solutions to the Helmholtz equation 2.4 with a Gaussian amplitude distribution can be obtained which define the spatial propagation of a wave in free space. For the derivation of a Gaussian wave refer to [7, p. 356-362]. The general form of a Gaussian beam is given by

$$\boldsymbol{E}(r) = \boldsymbol{E}_0(r, z) \exp\Big(- \frac{r^2}{W^2(z)}\Big), \tag{2.7}$$

where $r = \sqrt{x + y}$ is the distance from the beam center, and $W(z)$ is the beam width as illustrated in figure 2.2, defined by

$$W^2(z) = W_0^2 \Big[1 + \Big(\frac{z}{z_R}\Big)^2\Big], \tag{2.8}$$

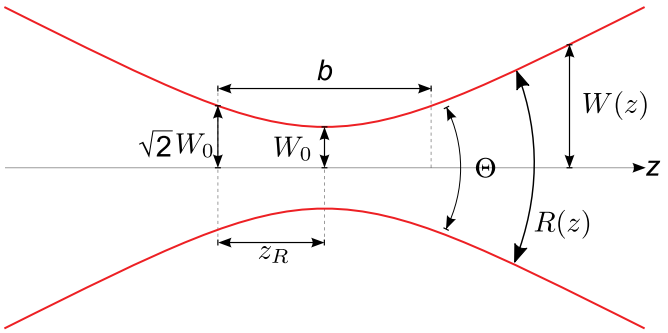

Figure 2.2: Gaussian beam width along the beam propagation axis z. Θ is the *divergence angle* given by $\Theta = \frac{2\lambda}{\pi W_0}$. b is the *confocal beam parameter* ($b = \frac{2\pi W_0^2}{\lambda}$) which is twice the *Rayleigh range* (z_R). Figure adapted from [6]

where W_0 is the minimum at the plane $z_0 = 0$, given by $W_0 = \sqrt{\frac{2z_R}{k}} = \sqrt{\frac{\lambda_0 z_R}{n\pi}}$, where z_R is the *Rayleigh range*, k is the wave vector, and λ_0 is the wavelength in vacuum. W_0 is known as the waist radius. The spot size is then given by $2W_0$, and

$$\boldsymbol{E}_0(r,z) = \frac{1}{W(z)}\Big[\frac{\sqrt{2}r}{W)}\Big]^m \boldsymbol{L}_l^m\Big(\frac{2r^2}{W^2(z)}\Big) \times e^{im\phi} \exp\Big[i\Big(\Phi(z) + \frac{kr^2}{2\boldsymbol{R}(z)}\Big)\Big], \tag{2.9}$$

where $\boldsymbol{R}(z) = z\Big[1 + \Big(\frac{\boldsymbol{z}_R}{z}\Big)^2\Big]$ is the radius of curvature and Φ is the Gouy phase given by

$$\Phi(z) = -(2l + m + 1)tan^{-1}\Big(\frac{z}{z_R}\Big). \tag{2.10}$$

In equation 2.9, $\boldsymbol{L}_l^m$ is the generalized Laguerre polynomials with l and m representing different spatial modes of a Gaussian beam which are illustrated in figure 2.3.

2.1.2 Intensity and Power

The intensity of a Gaussian beam is given by

$$\boldsymbol{I}(r,z) = \boldsymbol{I}_0 \exp\big(-2\frac{r^2}{W^2(z)}\big) \tag{2.11}$$

with

$$\boldsymbol{I}_0 = |E_0|^2\big(\frac{W_0}{W(z)}\big)^2. \tag{2.12}$$

The optical power of a Gaussian beam is

$$\begin{aligned} P &= \int_0^\infty \boldsymbol{I}(r,z) 2\pi r dr \\ &= \frac{1}{2}\boldsymbol{I}_0 \pi W_0^2. \end{aligned} \tag{2.13}$$

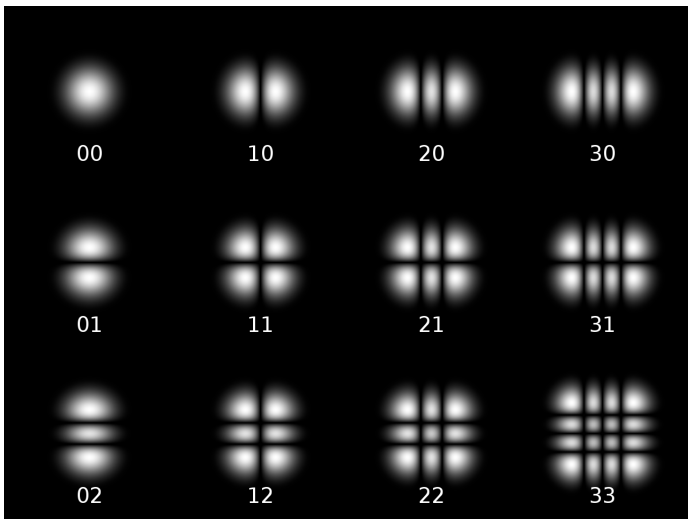

Figure 2.3: Gaussian Beam modes with different l and m values. Each mode is represented by TEM_{lm}. Figure taken from [8]

which is the integral of the intensity on a transverse plane at position z.

2.2 Mathematical Description of Ultra-short Pulses

In the simplest form, the temporal dependencies of a linearly polarized optical pulse in a fixed point in space can be considered. Neglecting the variation of the magnetic field in space relative to the electric field, this pulse can be described by the product of a time-dependent envelope function ($\boldsymbol{A}$(t)) and a carrier harmonic wave with the angular frequency ω_0 and the phase $\phi(t)$:

$$\boldsymbol{E}(t) = \boldsymbol{A}(t)\cos(\phi(t) + \omega_0 t). \tag{2.14}$$

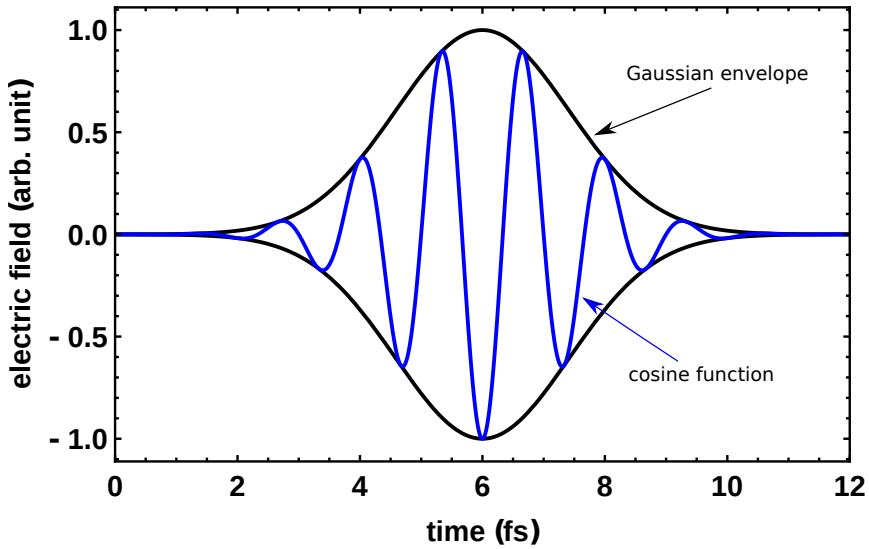

Figure 2.4: A Gaussian pulse

The intensity of this pulse at any point in time is given by

$$I(t) = \epsilon_0 nc\boldsymbol{A}^2(t)\cos^2\big(\omega_0 t - \phi(t)\big), \tag{2.15}$$

where n is the refractive index. The averaged temporal intensity is

$$\big\langle I(t)\big\rangle = \frac{1}{2}\epsilon_0 nc\boldsymbol{A}^2(t). \tag{2.16}$$

For convenience, the complex representation of the electric field can be used:

$$\boldsymbol{E}(t) = 1/2\big(\boldsymbol{E}(t)^+ + \boldsymbol{E}(t)^-\big), \tag{2.17}$$

with

$$\boldsymbol{E}^+(t) = \boldsymbol{A}(t)e^{-i\left(\omega_0 t - \phi(t)\right)}, \tag{2.18}$$

and

$$\boldsymbol{E}^-(t) = \boldsymbol{A}(t)e^{i\left(\omega_0 t - \phi(t)\right)}, \tag{2.19}$$

The complex electric field has a Fourier decomposition into monochromatic waves as follows

$$\boldsymbol{E}^+(t) = \frac{1}{2\pi}\int_{-\infty}^{+\infty}\widetilde{\boldsymbol{E}}^+(\omega)e^{i\omega t}d\omega, \tag{2.20}$$

$$\boldsymbol{E}^-(t) = \frac{1}{2\pi}\int_{-\infty}^{+\infty}\widetilde{\boldsymbol{E}}^-(\omega)e^{i\omega t}d\omega. \tag{2.21}$$

By analogy, the electric field in frequency domain is given by

$$\widetilde{\boldsymbol{E}}(\omega) = \widetilde{\boldsymbol{A}}(\omega)e^{i\phi(\omega)}. \tag{2.22}$$

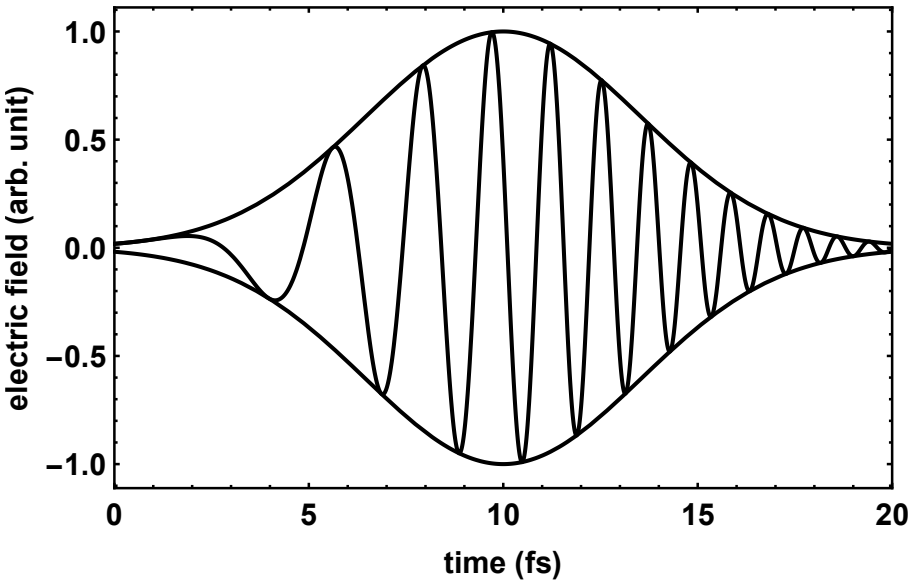

Figure 2.5: A pulse whose instantaneous frequency is increasing over time. This pulse is called to have a positive chirp.

Both representations are connected by the Fourier transform:

$$\widetilde{\boldsymbol{E}}^{+}(\omega) = \mathcal{F}(\boldsymbol{E}^{+}(t)) = \int_{-\infty}^{+\infty} \boldsymbol{E}^{+}(t) e^{-i\omega t} dt, \tag{2.23}$$

$$\widetilde{\boldsymbol{E}}^{-}(\omega) = \mathcal{F}(\boldsymbol{E}^{-}(t)) = \int_{-\infty}^{+\infty} \boldsymbol{E}^{-}(t) e^{-i\omega t} dt. \tag{2.24}$$

2.2.1 Phase and Chirp

The instantaneous frequency of a chirp-free pulse is the derivative of the phase with respect to time.

$$\omega(t) = \frac{\partial \phi(t)}{\partial t} = \omega_0, \tag{2.25}$$

ω_0 being the carrier frequency. If the pulse phase has a quadratic term, e.g., as a result of traveling in a non-linear medium, the phase will be a varying function of time

$$\omega(t) = \frac{\partial \phi(t)}{\partial t} = \omega_0 + \alpha t. \tag{2.26}$$

In this case, the frequency of the pulse is no longer constant and the pulse is said to be chirped. As an example, a pulse with a positive chirp is illustrated in figure 2.5 whose frequency increases with time.

2.2.2 Duration and Spectral Width Relationship

Usually, unless specified, pulse duration ($\Delta\tau$) is defined as the full width at half maximum (FWHM) of the intensity,$|\boldsymbol{E}(t)|^2$, and spectral width ($\Delta\omega$), FWHM of the spectral intensity $|\boldsymbol{E}(\omega)|^2$.These two quantities are related by the following relationship

$$\Delta\omega\Delta\tau \geq 2\pi K, \tag{2.27}$$

with K being a positive number on the order of 1 which depends on the actual pulse shape. Values of K for different pulse shapes are given in the following table:

Shape	K
Gaussian	0.441
Sech	0.315
Lorentzian	0.142

For a pulsed Gaussian beam the instantaneous power can be approximated by a Gaussian function:

$$\boldsymbol{P}(t) = \boldsymbol{P}_0 \exp\big(-4\ln 2(\frac{t}{\tau})^2\big), \tag{2.28}$$

with P_0 being the peak power.

The peak power [3] can be obtained in the following way:

$$\boldsymbol{P}_0 = \frac{\epsilon}{\int_{-\infty}^{+\infty} \exp\big(-4\ln 2(\frac{t}{\tau})^2\big)dt} = \sqrt{\frac{4\ln 2}{\pi}}\frac{\epsilon}{\tau}, \tag{2.29}$$

with ϵ being the pulse energy.

2.3 Propagation of Ultra-short Pulses

Considering a Photonic crystal [9][10], the band structure is used to explain the propagation of electromagnetic waves in such crystals. Since short pulses have a much larger spectral width, a wide range of band gap energies is responsible for the interaction between pulses and the medium. Therefore, short pulses undergo much bigger phase distortion as they propagate through a dispersive medium compared to a monochromatic CW light with a much smaller spectral width. This phase dispersion would result in an increase in the pulse duration. Considering, for instance, the electric field of an optical pulse in the frequency presentation:

$$\widetilde{\boldsymbol{E}}(\omega) = \widetilde{\boldsymbol{A}}(\omega)e^{i\phi(\omega)}. \tag{2.30}$$

[3] not to confused with the average power, measured using a power-meter, which is the repetition rate times the pulse energy $\overline{\boldsymbol{P}} = R_{rep}\epsilon$.

We can expand the phase $\phi(\omega)$ around the central frequency ω_0 using Taylor series:

$$\begin{aligned}\phi(\omega) &= \sum_{n=0}^{+\infty} \frac{1}{n!}\phi_n(\omega-\omega_0)^n \\ &= \phi_0 + \phi_1(\omega-\omega_0) + \frac{\phi_2}{2!}(\omega-\omega_0)^2 + \frac{\phi_3}{3!}(\omega-\omega_0)^3 + \dots\end{aligned} \tag{2.31}$$

In the equation 2.31, ϕ_n terms define different variations of the pulse phase. The first term ϕ_0 is called the carrier-envelope phase (CEP) whose influence is shown in figure 2.6. In short pulses regime, where the pulse period and envelope duration are comparable, e.g., in the case of few-cycle pulses, the CEP plays an important role because the difference between pulse with different CEPs is much larger relative to its duration.

The second term ϕ_1, is known as the group dispersion (GD) which adds a spectral phase factor. GD is a linear function of the frequency and does not have any effect on the pulse duration, but should be taken into account as the overlap of two pulses is important, for instance in pump-probe experiments.

ϕ_2, known as the group delay dispersion (GDD), introduces distortion in the envelope and the phase of the pulse resulting in the pulse length broadening. In the case of having only ϕ_0 and ϕ_1(instantaneous frequency constant in time), the pulse is called Fourier-limited where the pulse is the shortest. In this case, the equation 2.27 turns into

$$\Delta\omega\Delta\tau = 2\pi K. \tag{2.32}$$

2.3.1 Non-Linear Medium

In the presence of high-intensity pulses, the properties of the medium change. Generally speaking, a non-linear medium is characterized as a medium whose optical properties depend on the intensity of the electromagnetic fields passing through it. As a result, many effects can emerge, e.g. second harmonic generation, frequency conversion, parametric amplification, and parametric oscillation. The essential effects of non-linearity, that we are dealing with as regards ultra-short pulses, are the Kerr lens effect and self-phase modulation, as they are the main mechanisms for the creation of such pulses, e.g. in the mode-locking principle and the temporal compression in a hollow-core fiber.

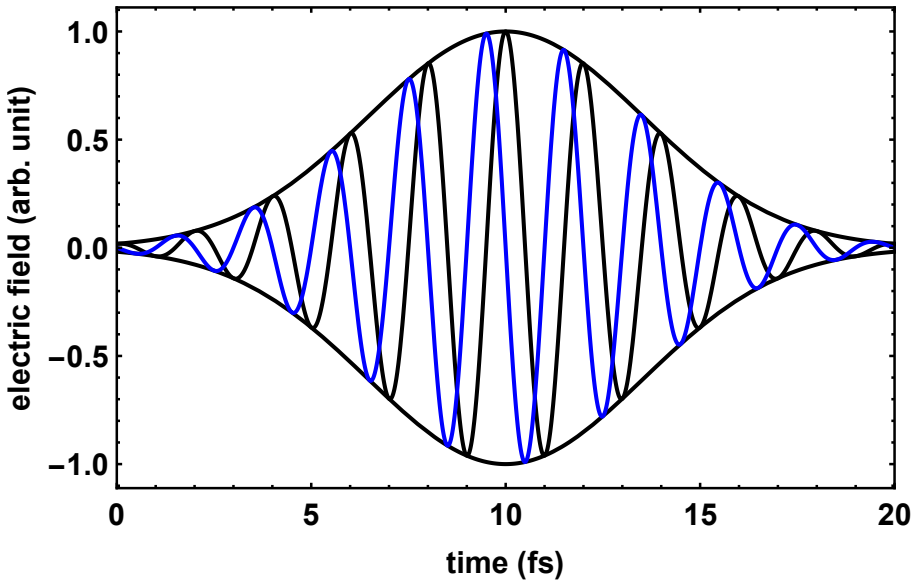

Figure 2.6: Carrier-envelope phase. The black line shows a pulse with $\phi_0 = 0$ and the blue line $\phi_0 = \frac{\pi}{2}$.

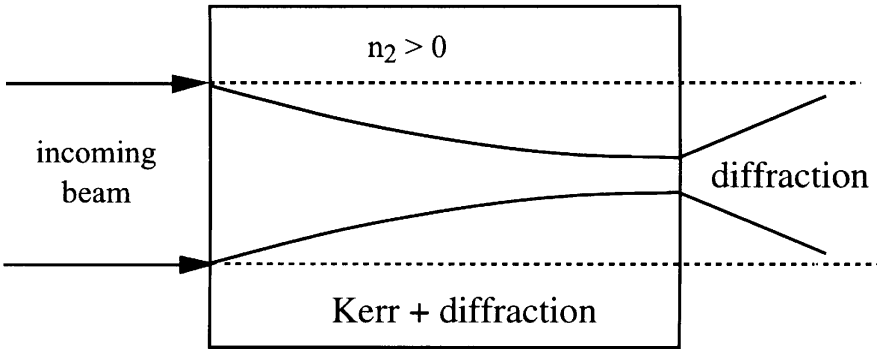

Figure 2.7: Self-focusing of a Gaussian beam through a nonlinear medium. Figure taken from [11]

2.3.2 Kerr Effect and Self-focusing

The change in the refractive index of a medium in response to the applied electric field is called the Kerr effect:

$$n = n_0 + n_2 I(t), \tag{2.33}$$

with n_0 being the refractive index of the medium without the presence of a high-intensity field, and $I(t)$ is the laser intensity.
Since n_2 is generally a positive number, the total refractive index n increases with intensity usually in the beam center and results in self-focusing as illustrated in figure 2.7.

2.3.3 Self-phase Modulation

Self-phase modulation (SPM) refers to the modification of an optical field phase as a result of the Kerr effect. SPM can be used as a technique to compress the pulse duration. If for instance, a laser beam passes through a non-linear medium, it can acquire different frequency components due to the Kerr effect. To proof this we can consider the intensity profile of a Gaussian beam in the time representation:

$$I(t) = I_0 e^{-4ln2\frac{t^2}{\tau^2}}. \tag{2.34}$$

As the pulse travels a distance L, the non-linear phase shift of the pulse is given by

$$\Phi(t) = \frac{\omega}{c} n_2 I(t) L. \tag{2.35}$$

Since the intensity is a varying function of time, so is the phase shift which results in a time-dependent frequency deviation:

$$\Delta\omega(t) = \frac{\omega}{c} n_2 L \frac{\partial I}{\partial t}. \tag{2.36}$$

One can estimate the spectral broadening of the pulse in the following way

$$\Delta\omega(t) = \frac{\omega}{c} n_2 L \frac{I_0}{\tau}. \tag{2.37}$$

where τ is the pulse duration. According to the above equation, pulse broadening is inversely proportional to the pulse duration which shows the importance of the incoming pulse duration for a maximum temporal compression.

2.4 Generation of Ultra-short Pulses

In this section methods that are routinely used to create ultra-short pulses on the time scale of a couple of fs are explained.

2.4.1 Mode-locking

Since the laser discovery in 1964, the usual technique to reach short pulses was to couple longitudinal modes of the laser cavity by phase synchronization of modes. This technique is called mode-locking whose goal is release the energy stored in the laser cavity in a short amount of time as illustrated in figure 2.8.. By introducing an intensity-dependent gain or loss in the laser gain medium, spikes of mode-locking can be favored in the cavity. This instantaneous gain or loss control can be achieved using a passive absorber or by the help of non-linear lenses, or actively, using acousto-optic or electro-optic modulators. The Kerr lens effect, as a passive absorber, is favored over other methods for its fast response allowing the production of short pulses.

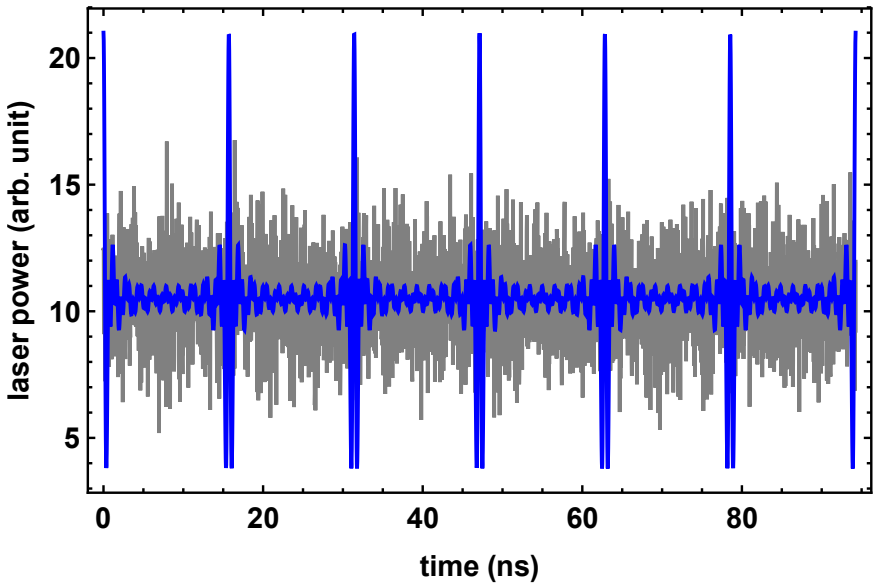

Figure 2.8: Mode-locking. In black: free-running modes are shown which oscillate independently. In blue, these modes oscillate with their phases being locked together. Peaks are distanced by the Fabry-Perot inter-modal relation $\nu_f = \frac{c}{2L}$ with L being the length of the laser cavity

2.5 Chirped-pulse Amplification

Since the introduction of Chirped-Pulse Amplification (CPA) in 1985 [12], this method has become the workhorse for high-intensity pulse production. This method is explained in chapter 5 along with the laser system.

2.5.1 Temporal Compression Using Hollow-core Fiber

In 1996, a novel spectral compression technique was introduced by Nisoli [13] which resulted in pulses with shorter duration. In this technique, pulses are sent through a hollow-cylindrical-fused-silica fiber filled with a noble gas. As a high-intensity laser passes through the fiber, nonlinear effects cause spectral broadening owing to self-phase modulation. Due to the intensity-dependent index of refraction in the Kerr effect, new spectral components are created which broaden the bandwidth. Afterwards, the introduced chirp is compensated using suitable phase-dispersive elements which results in shorter pulse durations. The principle of lights passing through a hollow-core fiber is the opposite of normal glass wires used in communication where the refractive index is higher in the middle. This can be viewed as multiple reflections from a dielectric surface of the inner wall at grazing incidence. These reflections can favour one particular mode.

3 Photoionization

Photoionization refers to a process where the electromagnetic field of a laser causes one or more electrons to escape the atom. Different processes are responsible for ionization, e.g. one-photon single ionization or double-ionization and ionization of atoms in a strong laser field. Single-photon ionization(SPI) takes place as the atom absorbs a photon which has more energy than the ionization potential of the target atom. The released photo-electron acquires almost all the energy difference between the ionization potential and the incoming photon (for complete treatment of the topic refer to [33][34][35]. In a strong laser field, however, two mechanisms are responsible for the ionization, namely, multi-photon ionization, or tunneling ionization. In the first case many photons can contribute to the ionization as shown in figure 3.2 a). In the latter, the Coulomb potential of the atom is distorted in the laser field allowing electrons to tunnel out the atom as illustrated in 3.2 b). SPI and strong-field ionization are illustrated in figure 3.1 where the momentum distribution of singly-charged helium ions ionized with one 85 eV photon of synchrotron radiation (left panel) or multiple 1.5 eV-photons from a laser field with an intensity of 1.5 $10^{15} \frac{W}{cm^2}$ (right panel) is shown. The momentum of photons in both cases can be neglected. Therefore, ion-electron pairs are emitted back-to-back (momentum conservation) which makes the momentum distribution image of electrons look almost like the mirror of that of ions shown in figure 3.1.

3.1 Single Ionization

Photoionization with an XUV photon takes place when an electron is ejected into the continuum state after absorbing a photon. The probability of such a transition per unit time is given by

$$P_{(photoionization)} \propto |M_{fi}|^2, \tag{3.1}$$

where M_{fi} is the matrix element of the interaction between the ground and continuum state. Considering the non-relativistic Hamiltonian for N-electron atom:

$$H = \sum_{i=1}^{N} \left(\frac{p_i^2}{2m} - \frac{Ze^2}{r_i}\right) + \sum_{j=1}^{N} \frac{e^2}{|\mathbf{r}_i - \mathbf{r}_j|}, \tag{3.2}$$

where the first two terms are the kinetic and potential energy of electrons, respectively in the field of the nucleus. The third term is the repulsive coulomb interaction between electron pairs. For a general treatment, one can introduce a plane polarized

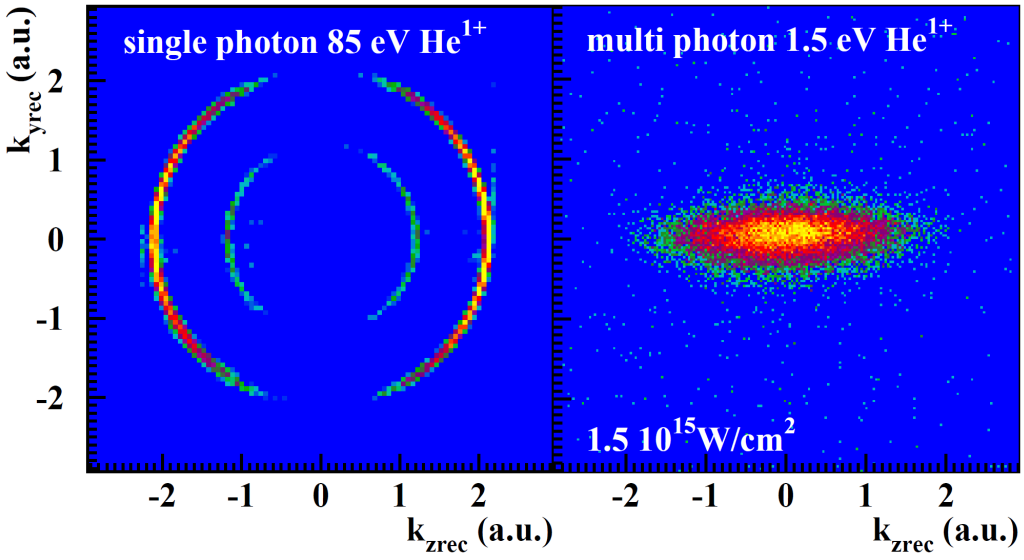

Figure 3.1: Momentum distribution of He^+ ions during single-ionization with the light polarization vector along the z axis. The left panel shows single-ionization using one photon. The right panel shows multi-photon ionization in a strong laser field. Figure taken from [1]

field in the form of

$$\mathbf{A}(\mathbf{r},t) = \hat{\mathbf{e}}A_0\big(exp(i(\mathbf{k}.\mathbf{r}) - \omega t) + c.c.\big), \tag{3.3}$$

where $\hat{\mathbf{e}}$ is the polarization vector, $\mathbf{r}$ is the position vector, $\mathbf{k}$ is the wave vector, and *c.c.* is the complex conjugate. As the atom interacts with an electromagnetic field with the vector potential of $\mathbf{A}(\mathbf{r},t)$ the Hamiltonian takes the form of

$$H = \sum_{i=1}^{N}\Big[\frac{(\mathbf{p}_i + |e|\mathbf{A}(\mathbf{r},t))^2}{2m} - \frac{Ze^2}{r_i}\Big] + \sum_{j=1}^{N}\frac{e^2}{|\mathbf{r}_i - \mathbf{r}_j|} \tag{3.4}$$

with

$$\mathbf{p}_i = -i\hbar\nabla_i = -i\hbar\frac{\partial}{\partial\mathbf{r}_i}. \tag{3.5}$$

At low intensities, A^2 can be neglected [1] resulting in the atom-field Hamiltonian:

$$H_{int} = \sum_{i=1}^{N}\Big\{\frac{|e|}{2m}[\mathbf{p}_i.\mathbf{A}(\mathbf{r}_i,t) + \mathbf{A}(\mathbf{r}_i,t).\mathbf{p}_i]\Big\}. \tag{3.6}$$

Choosing the coulomb gauge

$$\nabla.\mathbf{A} = 0, \tag{3.7}$$

[1] This term accounts for two-photon processes and is smaller at low intensities compared with single-photon ones

results in:

$$H_{int} = \sum_{i=1}^{N} \frac{|e|}{m} \mathbf{A}(\mathbf{r}_i, t).\mathbf{p}_i. \tag{3.8}$$

In order to satisfy the equation 3.7 one can set $\mathbf{k}.\hat{\mathbf{e}} = 0$ which means the polarization of the laser field is perpendicular to $\mathbf{k}$ and the field is transverse.
For simplicity, ground and continuum states in the hydrogen atom are only described here. The solution to the time-dependent Schrödinger equation

$$i\hbar \frac{\partial \Psi(\mathbf{r}, t)}{\partial t} = [H_0 + H_{int}]\Psi(\mathbf{r}, t), \tag{3.9}$$

where

$$H_0 = -\frac{\hbar^2}{2m}\nabla^2 + \frac{-Ze^2}{4\pi\epsilon_0 r}, \tag{3.10}$$

and

$$H_{int} = \frac{|e|}{m} \mathbf{A}(\mathbf{r}, t).\mathbf{p}. \tag{3.11}$$

can be given by

$$\Psi(\mathbf{r}, t) = \psi_{nlm}(r) e^{-iE_n t/\hbar}. \tag{3.12}$$

The bound wave function ψ_{nlm} can be written in spherical coordinate as the product of a radial and angular functions:

$$\psi_i(r, \phi, \theta) = \mathbf{R}_{nl}(r)\mathbf{Y}_l m(\phi, \theta). \tag{3.13}$$

In the continuum, the wave function can be expressed as

$$\psi_f(r, \phi, \theta) = \mathbf{R}_{\epsilon l}(r)\mathbf{Y}_{lm}(\phi, \theta), \tag{3.14}$$

where ϵ is the energy of the electron in the continuum, but still in the field of the nucleus [2]. The transition rate in the Hydrogen atom from the ground state to the continuum using the perturbation theory is given by

$$W_{fi} = 2\pi |M_{fi}|^2 \delta(E_f - E_i - \omega), \tag{3.15}$$

where E_f and E_f are the energies of the final and the initial states respectively. The matrix element is given by

$$M_{fi} = \langle \psi_f | \, H_{int} \, | \psi_i \rangle \,, \tag{3.16}$$

Using

$$\mathbf{E}(\mathbf{r}, t) = \frac{-1}{c} \frac{\partial \mathbf{A}(\mathbf{r}, t)}{\partial t}, \tag{3.17}$$

[2] The assumption is that the nucleus is infinitely heavy, but when the ejection energy is very high ($\epsilon \gg E_{1s}$) the resulting electron can be described by a plane wave

the matrix elements takes the form

$$M_{fi} = \hat{\mathbf{e}}\frac{E_0}{\omega}\langle\psi_f|\, exp(i\mathbf{k}.\mathbf{r})\nabla\,|\psi_i\rangle \tag{3.18}$$

where E_0 is the electric field amplitude and ω is its frequency. By using the dipole approximation, the assumption of the polarization in z direction, and $\nabla = \mathbf{r}\omega$, one can get

$$M_{fi} = E_0\,\langle\psi_f|\, z\,|\psi_i\rangle \tag{3.19}$$

The differential cross section can be defined by

$$\frac{d\sigma}{d\Omega} = \frac{1}{N_{ph}} = 2\pi\omega^3|\,\langle\psi_f|\, z\,|\psi_i\rangle\,|^2 \tag{3.20}$$

where N_{ph} is the photon flux defined by the number of photons per unit area per unit time. Assuming a transition from the ground state of the hydrogen atom ($\psi_i = \psi_{100}$) to the continuum ($\psi_f = \psi_{\epsilon lm}$)

$$\langle\psi_f|\, z\,|\psi_i\rangle = \sum_{lm} a_{lm}\,\langle\mathbf{R}_{\epsilon l}(r)\mathbf{Y}_{lm}(\phi,\theta)|\, r\cos\theta\,|\mathbf{R}_{1s}(r)\mathbf{Y}_{00}(\phi,\theta)\rangle \tag{3.21}$$

the cross section can be given by

$$\frac{\partial\sigma}{\partial\Omega} = \frac{\sigma}{4\pi}(1+\beta(P_2(cos\theta)) \tag{3.22}$$

where P_2 is the Legendre polynomial, θ is the angle between polarization axis and the emitted electron, and β is the anisotropy parameter of the angular distribution of the photoelectron. Selection rules according to equation 3.21, are

$$\Delta l = \pm 1,\ \Delta m = 0; \tag{3.23}$$

3.2 Strong-Field Ionization

Two mechanisms can contribute to ionization in a strong laser field, namely, multi-photon and tunneling ionization. The dominance of each mechanism is defined by the Keldysh parameter.

3.2.1 Keldysh Parameter

Keldysh parameter is an adiabatic parameter used to categorize different mechanisms of ionization:

$$\gamma = \sqrt{\frac{I_p}{2\,U_p}}, \tag{3.24}$$

where I_p is the ionization potential and U_p is the *ponderomotive potential* which is the energy acquired by the electron traveling in an oscillating field given by,

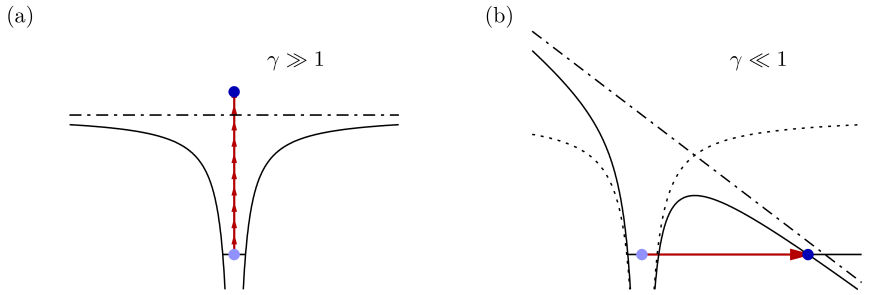

Figure 3.2: Ionization in a strong laser field. (a) Multi-photon ionization. (b) Tunneling of the electron as the atomic potential is affected by the laser field. Figure taken from [36]

$$U_p = \frac{e^2 E_0^2}{4m\omega^2} = \frac{e^2 I}{2m\epsilon_0 c\omega^2}, \tag{3.25}$$

where e is the electron charge, E_0 is the electric field amplitude, m is the electron mass, ω is the laser field frequency, ϵ_0 is the permittivity of the free space, and c is the speed of light.

At high intensities ($\gamma << 1$) 3.2b), tunneling ionization is the dominant mechanism as the laser period is longer than the electron tunneling time. At low intensities ($\gamma >> 1$) on the other hand 3.2a), the electric field of the laser changes faster than the tunneling time of the electron, and as a result the electron can absorb several photons to leave the atom.

3.3 Double Ionization with One Photon

Non-sequential double ionization takes place upon absorption of one photon which causes two electrons to be ejected from the atom. Due to the single-particle-photon nature of the photoionization, it can only take place as a direct result of electron-electron correlation. In other words, one photon interacts with the first electron, then the second electron is ionized as a consequence of their correlation. This correlation can be studied by considering two different models, namely, shake-off and knockout [37].

1. Knock-out

   As illustrated in figure 3.3, the first electron which absorbs a photon can knock the second electron out through electron-electron collision.

2. Shake-off

   During shake-off mechanism which is purely quantum mechanical, an electron escapes the atom very rapidly compared to the time scale of the bound electron. The remaining electron wave function now has to be projected onto the

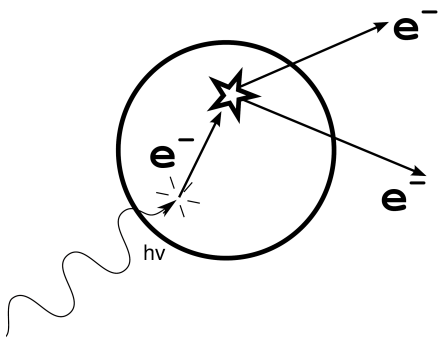

Figure 3.3: Knock-out mechanism where the first electron absorbs the a photon and gets accelerated out of the atom and on its way out it knocks the second electron out. Figure adapted from [38]

new ionic potential which has a new set of eigenstates (sudden approximation) which results in the projection onto some states being in the continuum. Therefore the electron is so-called shaken off the atom [39] [40].

3.4 Photoionization Time Delay

In 1948, the time delay in quantum mechanics was proposed by Eisenbund. He proposed that the time delay could be synonymous to the derivation of the phase shift with respect to energy [41]. Later, Wigner formulated time delays in quantum scattering, stating that the time delay can be defined as the derivative of the phase shift between two spherical waves. This phase shift results from the velocity change of a particle in the region of a potential. In the case of an attractive potential, as the particle approaches the potential it speeds up then slows down as the particle moves away. The induced phase shift can be formulated in the following way[42]

$$\delta(E) = \frac{1}{\hbar} \lim_{x\to\infty} \int_{-\infty}^{x} (p(x) - p_0)dx \tag{3.26}$$

and the delay can be written as

$$\tau_W = \hbar \frac{\partial \delta}{\partial E}, \tag{3.27}$$

The major challenge in measuring the time delay is that the time can not be measured directly during measurements. It is in fact the manifestation of a phase change in the electron wave packet and without a reference clock this is not meaningful. Therefore, coherent cross-correlation photo-electron spectra between XUV and a weak IR can be used to derive the time during photoionization. In 2007, a difference in photoionization time from different atomic states was shown using the streaking technique [43].

4 High Harmonic Generation

High harmonic generation refers to the process by which the interaction between a high-intensity laser field with a frequency of ω and a non-linear medium[1] results in the creation of the higher harmonics of the laser field, e.g. $2\omega, 3\omega, 4\omega, \ldots$. In 1961, P. A. Franken and his group succeeded in producing the second harmonic of their ruby optical maser by passing it through a crystalline quartz [15]. The interaction of a strong laser field with gases resulting in high harmonic generation was first observed by two different groups in 1987 [16][17].In 1992, Cy. Frakas and Cs. Tóth proposed high harmonic generation in a gaseous medium with a pulse duration of 30-70 as. They suggested that at high laser intensities $> 10^{13} W/cm^2$ the interaction of light and matter is no longer perturbative and the spectrum of high harmonics shows a plateau for many harmonics. Therefore, it was concluded that creating a short pulse with a spectral width of $\Delta\omega = 2N\omega$ (N being the number of odd harmonics) is feasible [18]. In 1999 N. A. Papadogiannis observed, for the first time, the localization of an attosecond pulse of high harmonics [19].
In figure 4.1 a typical spectrum of high harmonics created in a gaseous medium is shown. The characteristic of the spectrum is equidistant peaks at odd harmonics of the driving frequency ($(2n+1)\omega$). The spectrum comprises three regions:1) first few harmonics whose intensity drops rapidly, showing perturbative scaling which follows the I^q power law, with q being the harmonic order [20], 2) region of similar intensities or plateau 3) cut-off frequency which marks a sudden decrease of the intensity as illustrated in figure 4.1.

4.1 Three-Step Model

The semi-classical picture of high harmonic generation provides a good intuitive way of understanding this process [22]. It can also explain many characteristics of HHG including the cut-off frequency, different electron trajectories, and their phase evolution. According to this model, the electron can tunnel out, in the first step, of the atom when the potential of the atom, in the laser field, is distorted as illustrated in figure 4.2b). During the second step, the electron in the continuum gets accelerated in the laser field and can change direction as the sign of the electric field of the driving laser changes and recombines with the parent ion as shown in figure 4.2c). Upon recombination, the electron can release its energy, accumulated in the laser field, in the form of a photon in the soft x-ray region as shown in the figure 4.2d). These three steps repeat itself every half-a-cycle of the fundamental

[1] An ideal medium for high harmonic generation has to have a non-linear dielectric coefficient and also transparent to all the frequency passing through it. [15]

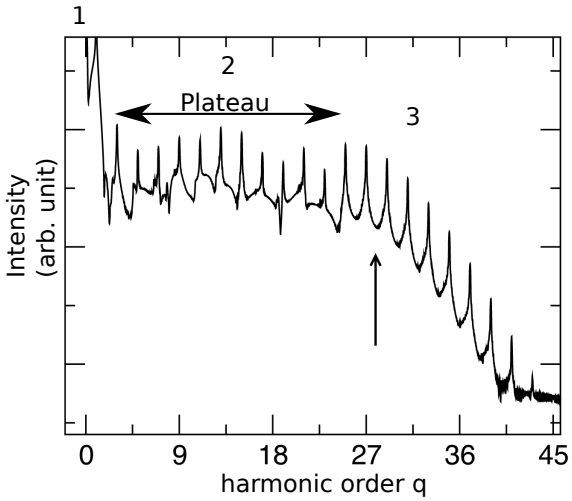

Figure 4.1: The spectrum of high harmonics. First harmonics show a sudden drop in intensity which originates from the perturbative nature of HHG in this energy range. The region of the constant intensity is called a plateau. The vertical arrow shows the cut-off region. Figure adapted from [14]

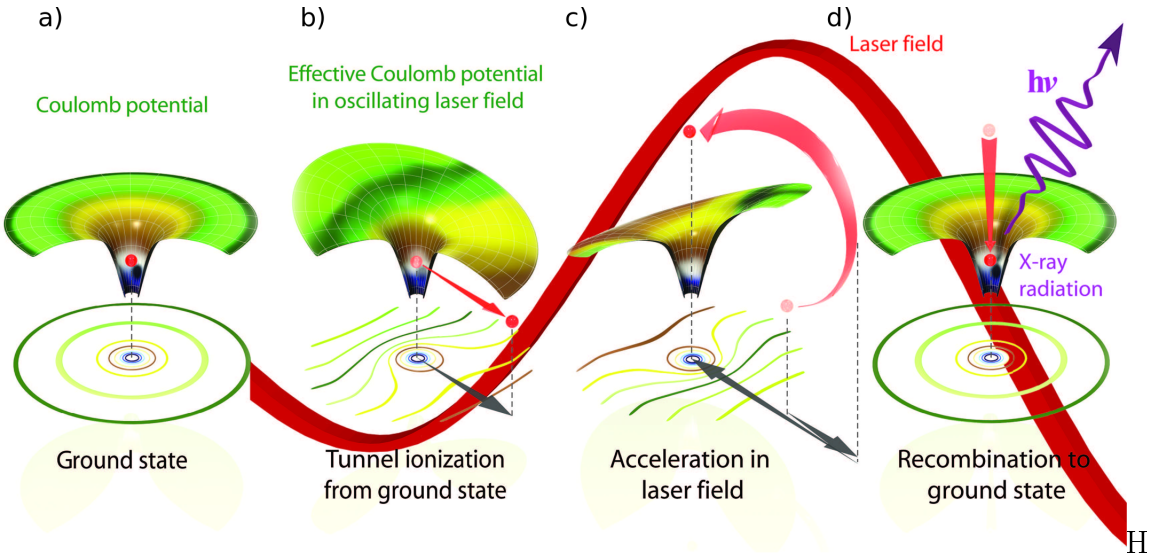

Figure 4.2: Three-step Model. a) the electron can tunnel out as the atomic potential gets bent in the strong laser field. b) The electron gets accelerated in the laser field. c) As the electric field of the laser field changes sign, the electron gets accelerated in the opposite direction. d) The electron hits the parent ion releasing its kinetic energy in the form of an XUV photon. Figure taken from [21].

laser field, resulting in equidistant spikes $2\omega_0$ apart in the frequency domain ($1\omega_0$, $3\omega_0$, $5\omega_0$, ...).[2] The effect of the electric field of the laser, which is the only force [3] affecting electrons as soon as they escape the nucleus, can be calculated using classical mechanics. Considering a linearly-polarized laser electric field,

$$\boldsymbol{E}(t) = \boldsymbol{A}_0 \cos(\omega t). \tag{4.1}$$

The electron is assumed to tunnel out with zero energy at time $t = t_i$. Solving the Newton equation of motion:

$$\boldsymbol{F}(t) = m\ddot{x} = q\boldsymbol{E}(t). \tag{4.2}$$

Integrating the above equation:

$$\dot{x} = \frac{e\boldsymbol{A}_0}{m\omega}\big[\sin(\omega t) - \sin(\omega t_i)\big], \tag{4.3}$$

$$x = \frac{e\boldsymbol{A}_0}{m\omega^2}\big[\cos(\omega t_i) - \cos(\omega t) - \omega(t - t_i)\sin(\omega t_i)\big], \tag{4.4}$$

As an electron travels in the laser field, it gains kinetic energy. The maximum energy that an electron can acquire in the laser field is 3.17 U_p where U_p is the *ponderomotive energy*, defined by

$$U_p = \frac{Ie^2}{2m_e\epsilon_0 c\omega^2} \propto \lambda^2 I. \tag{4.5}$$

The maximum photon energy or the *cut-off frequency* [4] is then given by

$$\hbar\omega_{cut-off} = I_p + 3.17U_p. \tag{4.6}$$

According to equation 4.4, the initial release time (t_i) results in different trajectories. As shown in fig 4.3a it can be seen that only electrons leaving the atom when the driving laser phase is between $\frac{T}{4}$ and $\frac{T}{2}$, return to the parent ion during a half-circle. It is also noticeable from 4.3b that two different sets of trajectories can end up with the same kinetic energy (shown with the vertical dashed line) known as long ($\frac{T}{4} < t_i < \frac{T}{3}$) and short trajectories ($\frac{T}{3} < t_i < \frac{T}{2}$).

[2] HH pulses repeat itself twice an optical cycle resulting in $T/2$ distance between peaks in time domain corresponding to $2\omega_0$ in frequency domain.

[3] At laser intensities below $10^{15}\frac{W}{cm^2}$ the relativistic effects and the effect of the laser magnetic field can be neglected

[4] $\omega_{cut-off}$ increases linearly with intensity, but at high intensities the cut-off frequency is smaller that the value from the equation 4.6 because of the saturation in the target which is more pronounced for long electron trajectories as the target can become fully ionized before the peak of the driving laser.

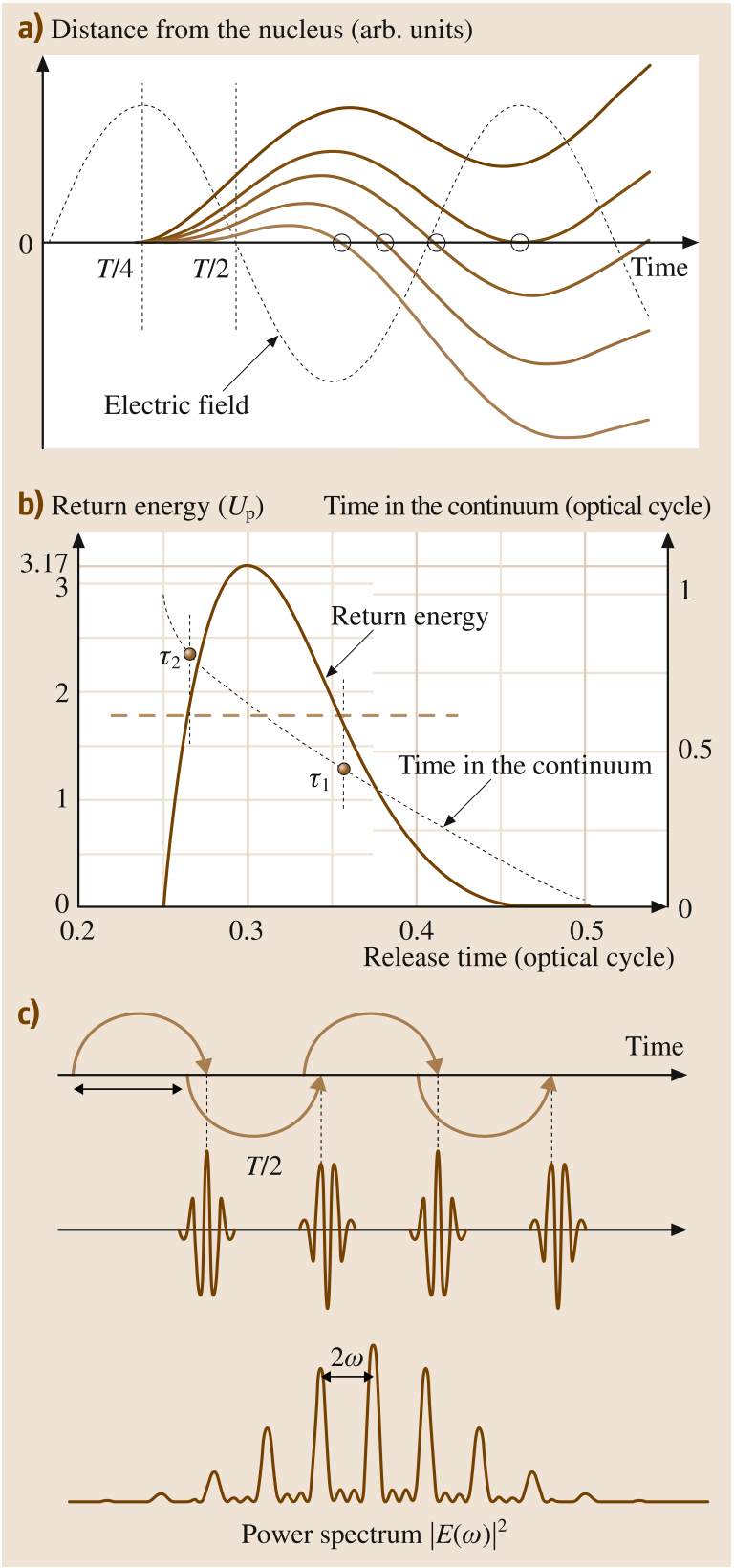

Figure 4.3: a) Different release time results in different trajectories. b) The solid line shows the kinetic energy and the dotted line the time in the continuum. c) The process takes place every half a cycle resulting in odd harmonic. Figure taken from [23]

4.2 Phase Matching

The characteristics of XUV pulses depend both on the single-atom response and the medium where HHG takes place [24][25] [26]. Phase matching deals with the effects of this medium on the resulting XUV pulses. High harmonics are generated in a non-linear medium. Therefore, each harmonic frequency has a different phase velocity. In order to create high harmonics with intensities enough to perform an experiment, the phase of each generated harmonic must match with that of the others so as to have constructive interference as shown in figure 4.4.
A useful quantity in phase-matching is the *phase mismatch* defined by

$$\Delta\mathbf{k} = q\mathbf{k}_0 - \mathbf{k}_q[27], \tag{4.7}$$

where $\mathbf{k}_0$ and $\mathbf{k}_q$ are the propagation vectors of the fundamental and qth harmonic respectively (for a complete derivation refer to [28]). In order to reach the ideal phase matching $\Delta\mathbf{k}$ should be zero.
The phase mismatch results mainly from three effects:

- Geometrical phase mismatch (Δk_g) caused primarily by the Gouy phase which is the rapid phase change of a Gaussian beam over the focus according to equation 2.10. The Gouy mismatch is the limiting factor in reaching a perfect phase matching [29].

- Dispersion phase mismatch resulting from the generating medium (Δk_n) and free electrons (Δk_p). Free electrons resulting from the ionization of the driving laser cause a plasma with a refractive index for qth harmonic

$$n_q = \sqrt{1 - \left(\frac{\omega_p}{q\omega}\right)^2}, \tag{4.8}$$

  where $\omega_p = \sqrt{4\pi e^2 N_e m_e z}$ is the *plasma frequency*. Since $\frac{\partial n_q}{\partial \omega} < 0$, the dispersion of the generating medium ($\frac{\partial n}{\partial \omega} > 0$) can be compensated in an perfect phase matching.

- Atomic dipole phase mismatch (Δk_d) which comes from the acquired phase of the electron as it travels in the laser field.

In practice, changing the conditions like the wavelength, gas pressure, gas species, wave guide size, and the spatial mode, a near compensation for different mismatch contributions can be achieved:

$$\Delta k = \Delta k_g + \Delta k_p + \Delta k_n + \Delta k_d \approx 0. \tag{4.9}$$

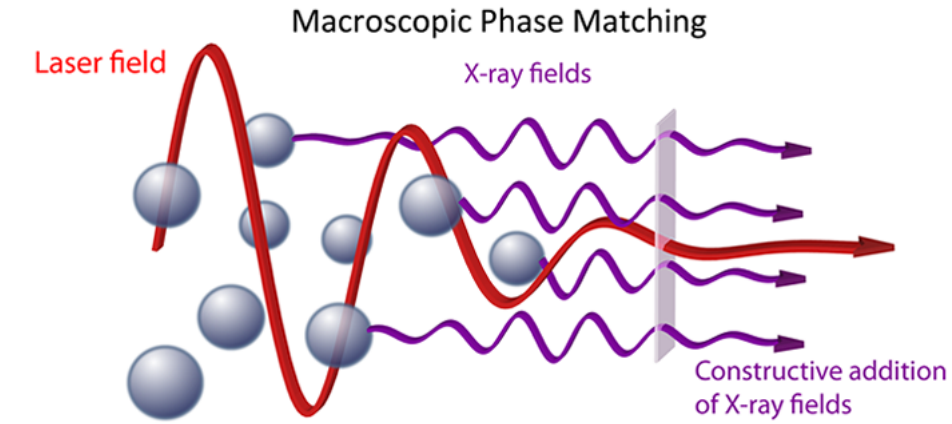

Figure 4.4: Phase matching of different harmonics. The vertical plane shows the position where different harmonics add constructively. Figure taken from [21]).

4.3 Attosecond Pulse Train and Its Characterization

The resulting XUV pulses from HHG can be treated either in the frequency or time domain. During HHG, short bursts of attosecond duration are created in each half cycle of the driving laser field. The interference of all these bursts results in harmonics and the sum of different harmonics creates an attosecond pulse train (APT) which can be treated either in the frequency or time domain [30]. The electric field of an APT is the coherent sum of the individual harmonic electric fields:

$$E_{APT} = \sum_{q} E_q(t) e^{-i\left(q\omega_0 + \phi_q(\omega)\right)}, \tag{4.10}$$

where ϕ_q is the phase of the qth harmonic. APTs in most cases are composed of harmonics with different phases (ϕ_q) which means that the APT is chirped ($\frac{\partial^2 \phi}{\partial \omega^2} \neq 0$) mostly positively at low enrgies because of the contribution of short trajectories. In order to calculate theses phases in an APT, a cross-correlation method known as RABITT is often used [31].

4.3.1 RABITT

In the RABITT (Reconstruction of Attosecond Beating By Interference of Two-photon Transitions) technique, an APT is cross-correlated with its fundamental laser field which results in the creation of side-bands between harmonic peaks in an APT. This method indirectly provides information about the phase of different harmonics. As an APT ionizes a medium in the presence of an IR field, photo-electrons can absorb or emit a photon of the fundamental laser which leave them

with the energy of:

$$E_{SB_{q\pm1}} = (q \pm 1)\hbar\omega_{IR} - I_p, \tag{4.11}$$

where I_p is the ionization potential of the gas target and q is the harmonic order. Therefore, side-bands are formed between harmonic peaks. Each of these side-bands can be reached from two adjacent harmonics. For instance, a photo-electron ionized by qth harmonic can absorb a fundamental photon and reach side-band q+1, or a photo-electron ionized by the q+2th harmonic can emit a photon and end up in side-band q+1. This effect will result in the interference of two quantum paths to a same final state (side-band) taken by photo-electrons as illustrated in figure 4.5. From these interferences information about the phase of the APT can be inferred. This technique was used for the first time, in 2001, to characterize an APT [32]. The intensity of side-bands depends on the time delay between APT and IR [32] as well as the matrix element of the two-photon transition:

$$I_{SB} \propto \cos\big(2\omega_{IR}(\tau + \tau_{XUV} + \tau_W)\big), \tag{4.12}$$

where τ is the time delay between pump and probe pulses, τ_W is the intrinsic atomic time delay resulting from the difference in transition amplitude phases of different quantum paths ending up to the side-bands which is the same as the Wigner time in the case of atoms, and τ_{XUV} is the group delay of the XUV pulse or the so-called attochirp given by:

$$\tau_{XUV} = \frac{\phi_{q-1} - \phi_{q+1}}{2\omega} \tag{4.13}$$

Although RABITT was original a tool to characterize APT, it is used in recent years to acquire information about photo-electron phase during photoionization.

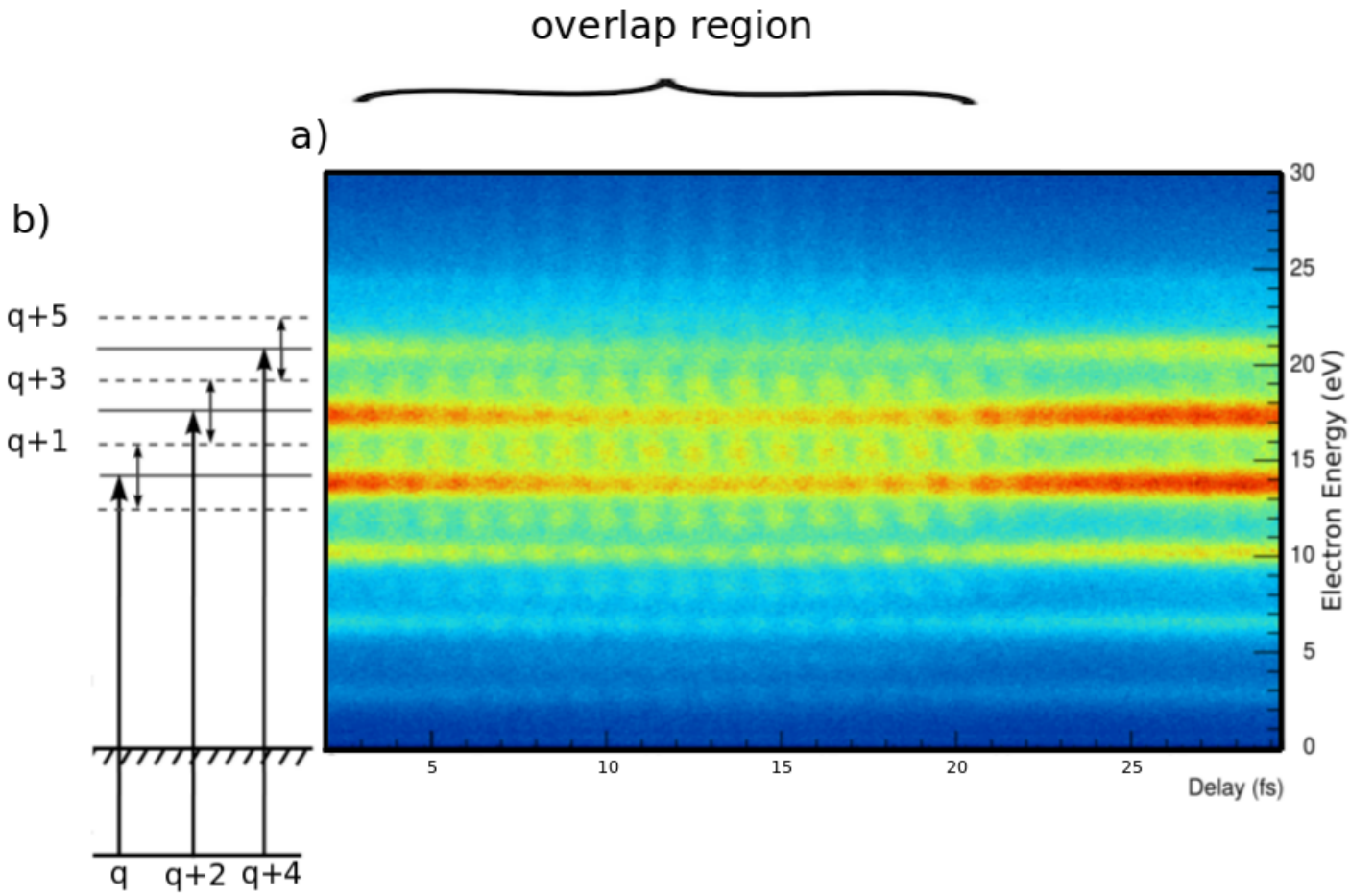

Figure 4.5: a) Photoionization of argon gas with an XUV in the field of IR. The energy of photo-electrons is plotted as a function of the XUV-IR delay. In the region where the two pulses overlap, a photo-electron can either absorb or emit a photon from the IR field resulting in the formation of sidebands between harmonic peaks which oscillate at the frequency of $2\omega_0$. b) Diagram of quantum interference illustrating the two paths leading to the same final state

5 The Laser System

5.1 Femtosecond Oscillator

A commercially available (KMLabs) Kerr-lens mode-locked oscillator, as shown in the green box in figure 5.1, provides pulses with a spectral width of around 60 nm at a central frequency of 790 nm which corresponds to a pulse duration of 16 fs (transform-limited). The gain medium is a Ti:Sapphire (Ti:Al2O3) crystal pumped by a frequency-doubled continuous-wave pump laser (Verdi V6, Coherent Inc.) with a wavelength of 532 nm. In mode-locked operation, the oscillator delivers an output power of 680 mW at a repetition rate of 80 MHz corresponding to a pulse energy of 9 nJ.

5.2 Chirped Pulse Amplification Amplifier

The incoming pulses from the oscillator do not have enough energy to perform the desired experiments. In order to amplify them, a multi-pass-chirped-pulse-amplification amplifier (KM Labs, Dragon CPA system) is used (blue parts in figure 5.1).
In the first stage, incoming short and low-energetic pulses are expanded in time to a couple of picoseconds through the stretcher, composed of a highly dispersive double-grating arrangement. The goal is to reduce the peak power of pulses so that during the amplification the gain medium would not get damaged. In the next stage, a Pockels cell is used so that the high repetition rate of the incoming pulses from the oscillator matches that of the pump laser (8 kHz).
In the next step, the stretched pulses go thirteen times through the Ti:Sapphire crystal which is cooled cryogenically. Upon each passage the pump pulse which is spatially and temporally matching IR pulses, amplifies them.
In the final stage, the long- and high-energetic pulses are compressed by a grating compression system. The resulting pulses have a duration of around 32 fs and a average power of 8 W at a repetition rate of 8 kHz.

5.3 Pulse Compression Using Hollow-core Fiber

So as to make the pulses even shorter in time and improve spatial properties of high harmonic generation [45], a combination of a hollow-core fiber with chirped mirrors is used. As pulses travel through the hollow core fiber, their spectral width increases as a result of self-phase modulation (SPM). The hollow-core fiber used

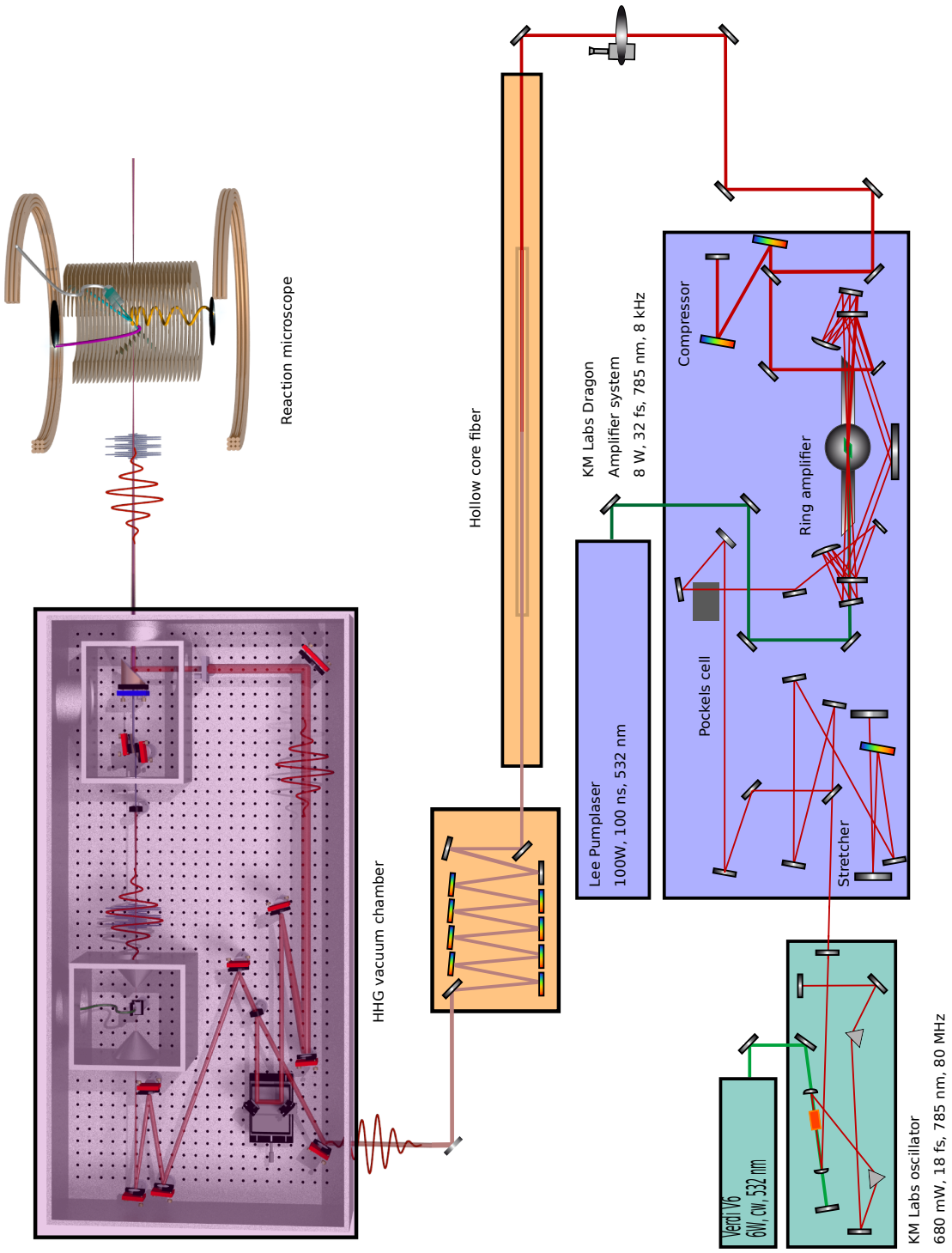

Figure 5.1: Experimental setup in Attolab at MPIK. The pulses, as short as 16 fs, are generated by a femtosecond oscillator pumped by Verdi V6 (green boxes). A CPA amplifying stage (blue boxes) amplifies pulses to the pulse energies of 1 mJ at a repetition rate of 8 kHz. Pulses are compressed in time by the help of a hollow-core fiber and a set of chirped mirrors (orange boxes). Figure taken from [44]

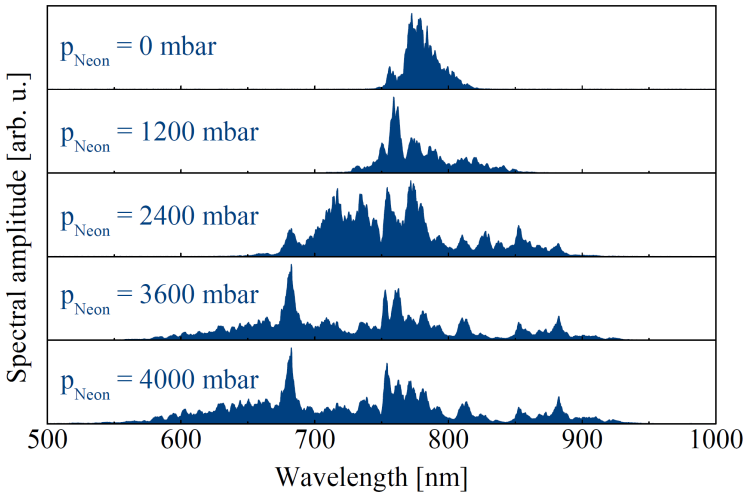

Figure 5.2: Spectral broadening in hollow-core fiber. The spectral width of the laser pulses is illustrated for different pressures of the neon gas in the fiber. Figure taken from [46]

at Attolab is 1 meter long and has a inner diameter of 250 μm and is filled with neon. The broadening of the spectral width for different gas pressures is illustrated in figure 5.2. After the hollow-core fiber pulses have already gained dispersion. To compensate for this dispersion a six-pair set of custom made chirped-mirrors is used (orange parts in figure 5.1). Each mirror introduces negative GDD to compensate for the dispersion from SPM, different glass windows, air, and the beam splitter in the experimental set-up.

5.4 Vacuum Chamber

In order to achieve stable and high quality pulses, a vacuum chamber is designed to cover both interferometric arms of the Pump-probe set-up as illustrated in figure 5.3. The following parts explain the main design.

5.4.1 Mach Zehnder Interferometer

A Mach-Zehnder interferometer is placed inside the vacuum chamber as illustrated in figure 5.3. The incoming beam is split using an 80:20 beam splitter creating pump and probe arms respectively.

In the pump arm, 80 percent of the beam power is used to create XUV pulses through high harmonic generation. To do so, the beam is focused, using a 50cm-focal-length spherical mirror, into a metal tube filled with argon as shown in figure 5.4. As a result, a train of XUV is produced with a typical spectrum shown in figure 5.4b). After the XUV generation, a gas filter absorbs the low-order harmonics as explained in the next section, then the driving laser beam is blocked by an aluminum

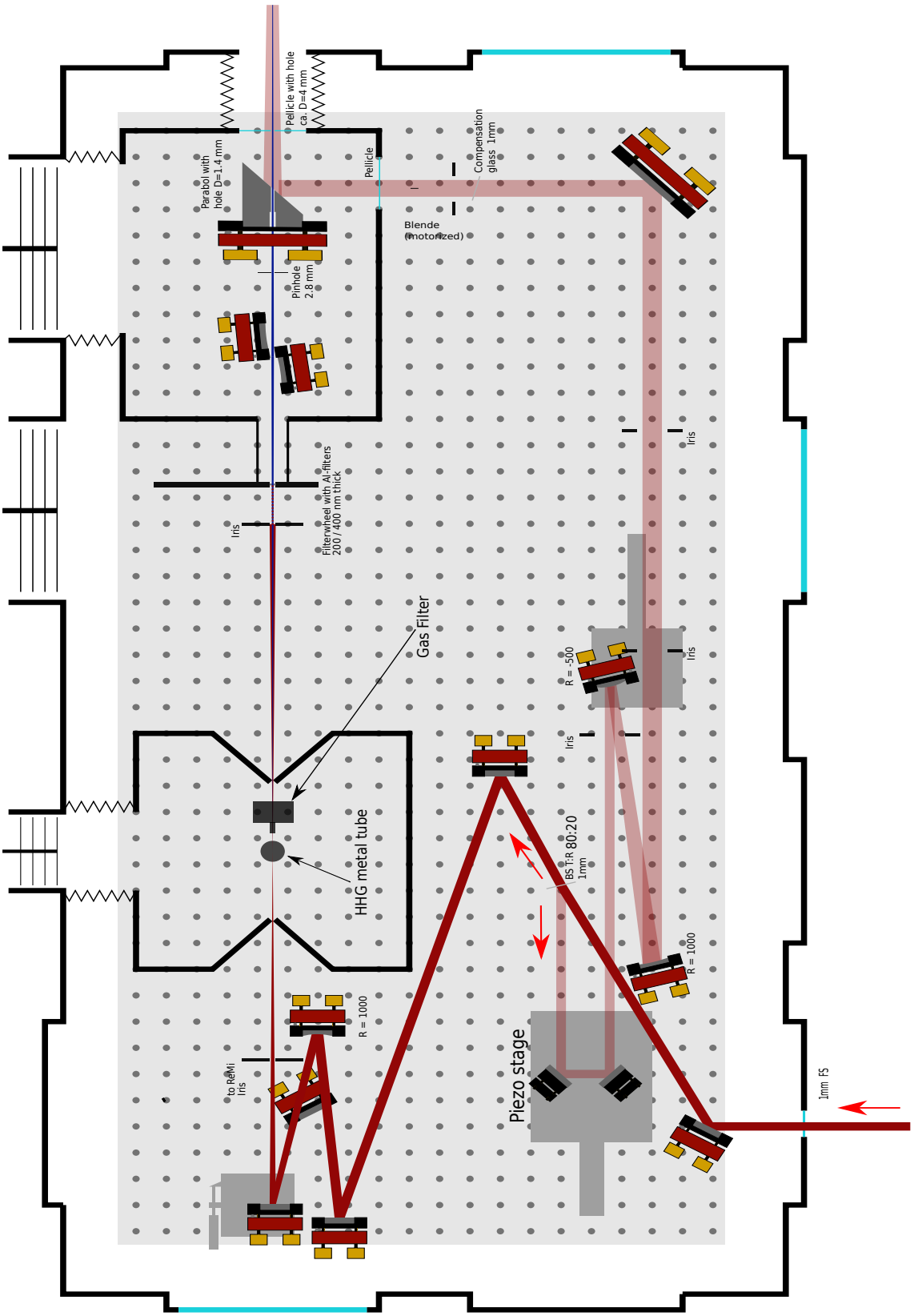

Figure 5.3: Mach-Zehnder interferometer inside the vacuum chamber. Figure adapted from [44]

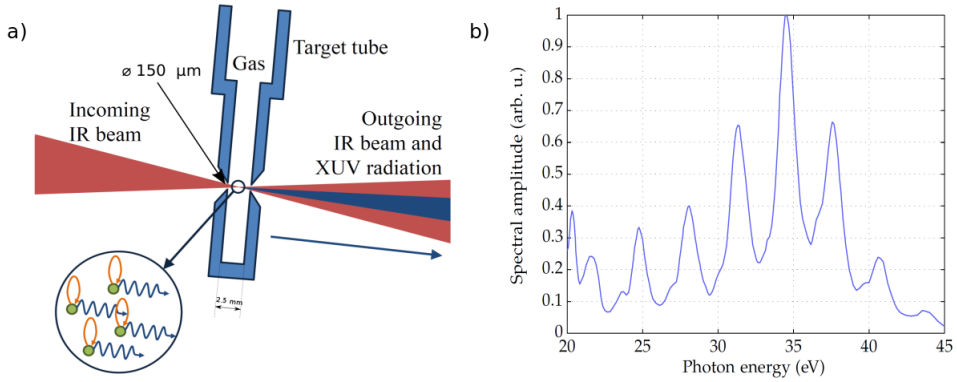

Figure 5.4: a) HHG generation metal tube. The laser is focused on a metal tube. The diameter of holes the laser going through is $150\mu m$ and interaction length $2.5mm$. b) A typical spectrum of HHG. a) Figure taken from [46] b) Figure taken from [47]

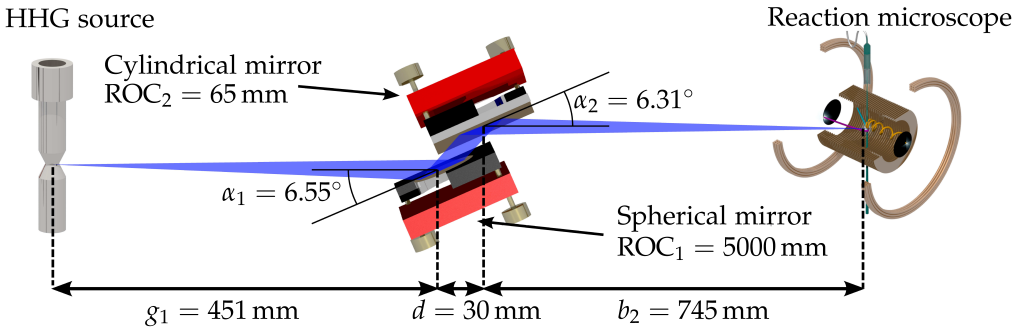

Figure 5.5: Focusing of XUV. Two mirrors were designed so that the beam is refracted under the grazing incidence. Figure taken from [44]

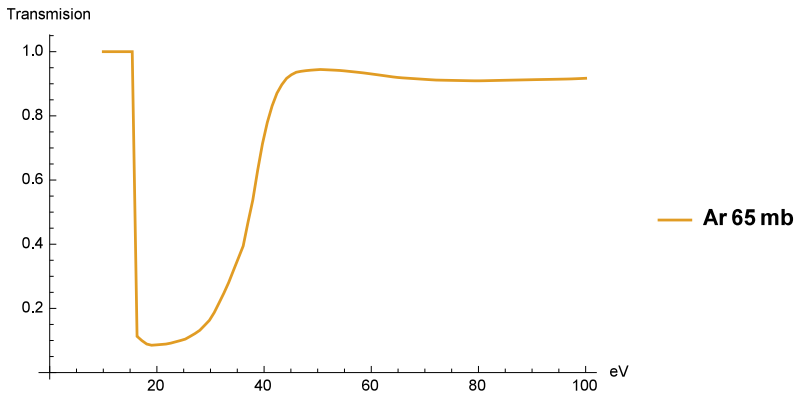

Figure 5.6: Transmission of argon gas used to filter lower-order harmonics and 200μm-thick aluminum filter used to block the fundamental IR after the HHG [48].

foil with a thickness of 200 μm. Ultimately, the remaining APT is focused on the center of the ReMi using a pair of boron-carbide coated cylindrical and spherical mirrors as shown in figure 5.5.
On the probe side, a piezo delay stage introduces delay in the pump arm. Eventually pulses are focused, using a parabolic mirror with a hole in the middle in order to let XUV-IR overlap, into the gas jet in the ReMi.

5.4.2 Filtering low energetic Photons with Gas Filter

For a precise measurement the number of photoionization events should not be too high, otherwise the detection and data acquisition systems would run into problems. Typically with argon in both HHG target and the ReMi, 7000 ionization events per second take place. Since the goal of this thesis is to investigate double-ionization, the ideal case would be to filter out low order harmonics in APT so as to reduce the count rate to the ideal count rates of around 1300 count/s while boosting the double- to single-ionization ratio. For this purpose, argon gas is used because of its transmission profile which has a high absorption coefficient at low photon energies as illustrated in figure 5.6. Argon is injected into a gas filter (shown in figure 5.7 b) which is placed 25 mm after the HHG target. As a result the lower harmonics are suppressed relative to the higher ones as shown in 5.7a).

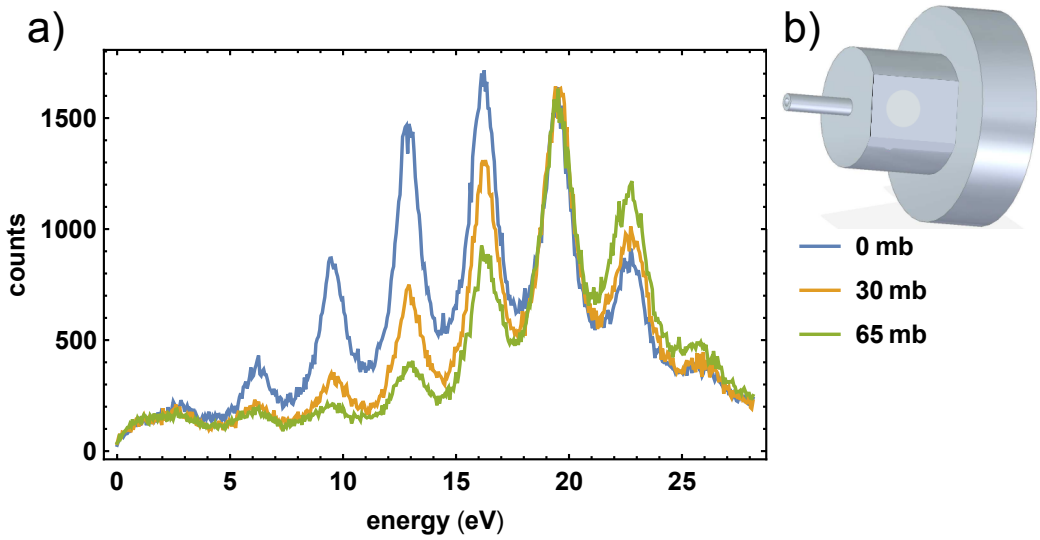

Figure 5.7: a)The spectrum of photo-electrons detected by the ReMi for different gas pressures. According to the transmission profile of the argon for XUV light as the pressure increases the lower oder harmonics are suppressed. All the curves are normalized to the peak at 19.2 eV. b) Gas filter with the length of 30 mm and diameter of 1.5 mm is placed 25 mm after the HHG target

6 Reaction Microscope

A Reaction Microscope (ReMi) is a powerful tool to perform recoil-ion and electron momentum spectroscopy with unprecedented precision. The main purpose of the ReMi is to perform momentum-resolved measurements of charged particles emerging from atomic and molecular fragmentations in an event-by-event manner to determine their momentum vectors [49]. This chapter covers the working mechanism and specifications of the ReMi.

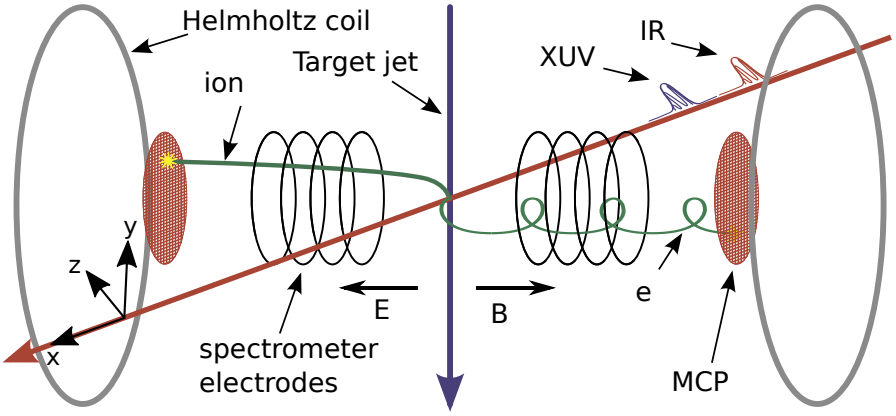

Figure 6.1: Reaction Microscope. A supersonic gas is used in the middle as the gas target. The laser beam ionizes the target. In the presence of the magnetic and electric field both ions and electrons fly in opposite directions towards the detectors. Using time of flight and particle position on the detectors, a full reconstruction of the momentum vectors is possible. Figure taken from [50]

6.1 Design and Mechanism

In our setup, focused short laser pulses are interacting with the supersonically-cooled gas target in the middle of the ReMi. The laser ionizes the target and created ions and electrons are directed, using the combination of a magnetic and electric field, towards the corresponding multi-channel plates (MCPs) and delay-line anodes which serve to determine the time of flight (TOF) and the position particles hit the detectors respectively. Finally, the momentum vectors can be reconstructed from the TOF and hit position. Following sections, explain in more detail the main components.

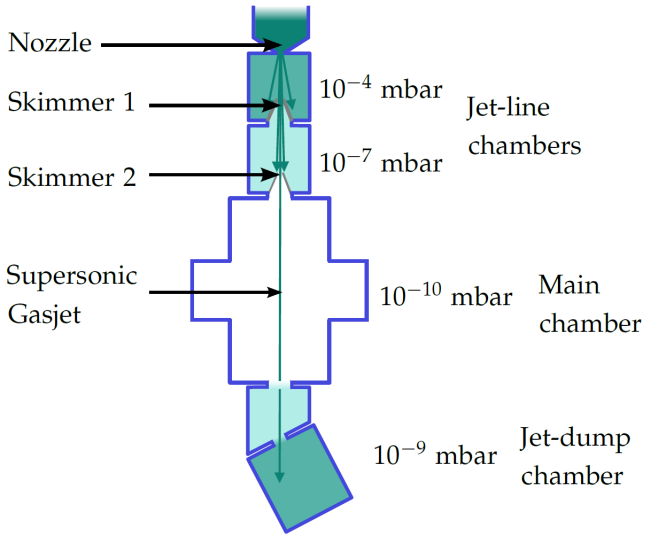

Figure 6.2: Gas jet stages. Figure taken from [44]

6.1.1 Gas Target

The gas target in the center of the ReMi has a very low temperature in order to have a good momentum resolution. Through supersonic expansion[51], the gas loses much of internal energy. For detailed description refer to [52]. The schematic of the gas jet vacuum stages is shown in figure 6.2. The gas at the room temperature with the stagnation pressure of 1 to 5 bar expands through a nozzle with the diameter of 30 μm into the first stage with a typical pressure of 1×10^{-4} mbar. A skimmer with a diameter of 200 μm separates the incoming gas from the warm background gas in zone of silence and guides it into the next stage with a pressure of 1×10^{-7} mbar. The last skimmer with a diameter of 400 μm let the gas into the main chamber of the ReMi with a typical pressure of 1×10^{-10} mbar. As a result, particles with a very small momentum distribution in the plane perpendicular to the propagation direction of the gas can be achieved which reduces the momentum uncertainty in momenta reconstruction processes.

6.1.2 Detection of Charged Particles

In the ReMi, two detectors serve to detect ions and electrons respectively. A combination of an electric and magnetic field is used so as to reach a near 4π solid angle acceptance. High resolution momentum construction requires near perfect homogeneous fields over the length of the spectrometer. A homogeneous electric[1] field is created using 32 equidistant spectrometer plates as shown in figure 6.3. Since photo-electrons have energies up to 40 eV, a homogeneous magnetic field, created by a pair of Helmholtz coils, is needed to confine almost all photo-electrons. Because of the very small charge-to-mass ratio of electrons, homogeneity of the magnetic field is

[1]For more information on the design of the spectrometer refer to [52]

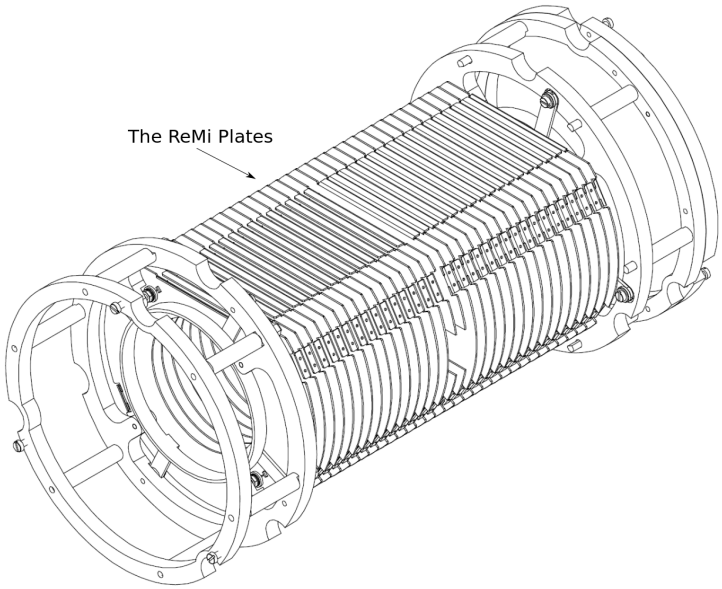

Figure 6.3: The reaction microscope plates. Figure taken from [53]

essential to the accurate reconstruction of the electron momentum. Helmholtz coils are, in our set-up, tilted to compensate the earth magnetic field.

Charged particles are then detected using MCPs with a diameter of 40 mm as illustrated in figure 6.4. The provided signal by MCPs is used to determine the TOF of the incoming particle using the following formula

$$ToF = T_{MCP} - T_{pulser} + T_0, \tag{6.1}$$

with T_{pulser} being the time acquired from a photo-diode triggered by each laser pulse and T_0 is the time offset to account for the signal delay in the electronic circuits. A typical ion time of flight is shown in 6.5. In order to determine the hit position on the detector, two sets of copper wires (delay-line anode) in a mesh form, biased positively with respect to the MCP, is placed behind the MCP as illustrated in figure 6.6. A signal is produced when an electron cloud, resulting from the electron avalanche, hits this mesh. The signal travels in both directions of each wire. It is then detected at each end. The time difference in the detected signal form each wire is used to calculate the hit position on the detector. In figure 6.8 both ion and electron detectors are shown.

6.2 Particle Momenta Reconstruction

With the TOF and hit position of charged particles, the information about the momentum vectors at the time of the reaction can be calculated. Starting with the

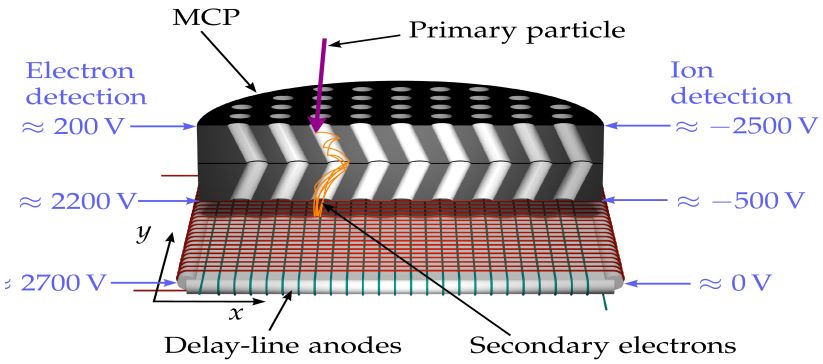

Figure 6.4: An MCP whose surface has many channels. The inner surface of each hole is covered with a semiconductor material which serves as an electron multiplier. As a charged particle enters an MCP hole, it accelerates in the electric field and hits the inner surface of it, and as a result, a secondary electron cloud forms after several collisions. These secondary electrons hit the delay line anode and causes a voltage drop which is used to calculate the hit position on the detector. Figure taken from [44]

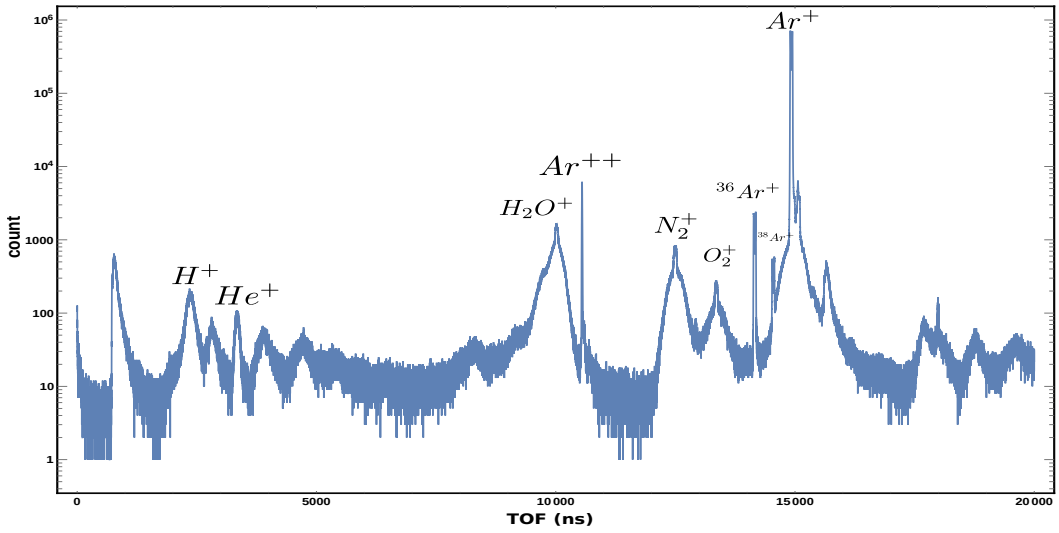

Figure 6.5: A typical ion time of flight. Different charge to mass ratios for various particles result in specific peaks for each particle. Broad peaks belong to the rest gas in the ReMi which are warmer than the gas target. The biggest peak belongs to the particles in the gas jet which is argon in this case. Smaller sharp peaks belong to the contamination of the gas jet with those particles.

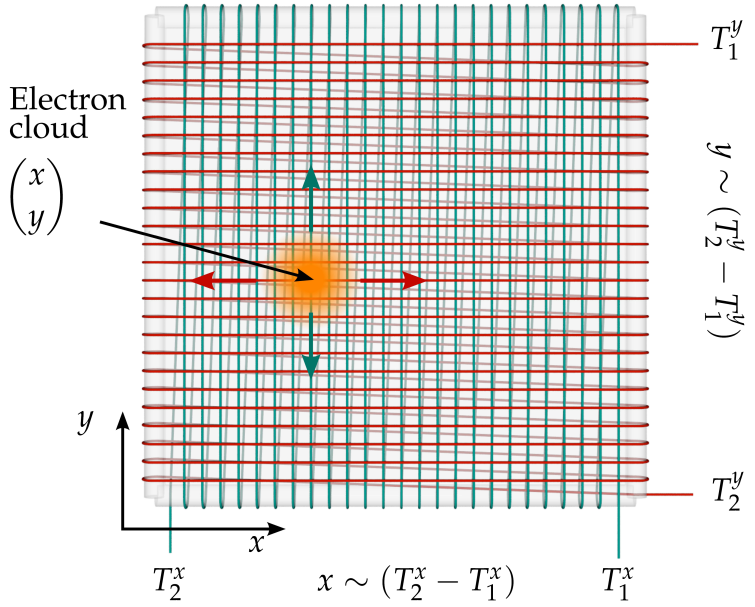

Figure 6.6: Delay line anode. The electron cloud created by the MCP generates a signal. It travels in the wires. The arrival time of the signal at each end of the wires can be used to calculate the electron cloud position. (Adapted from [44]).

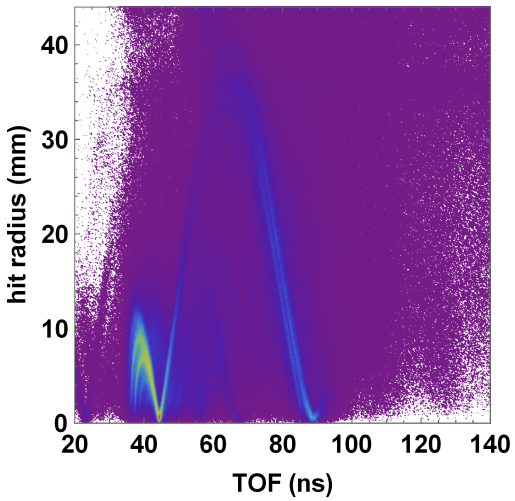

(a) The electron TOF as function of hit radius on the detector ($R = \sqrt{x^2 + y^2}$).

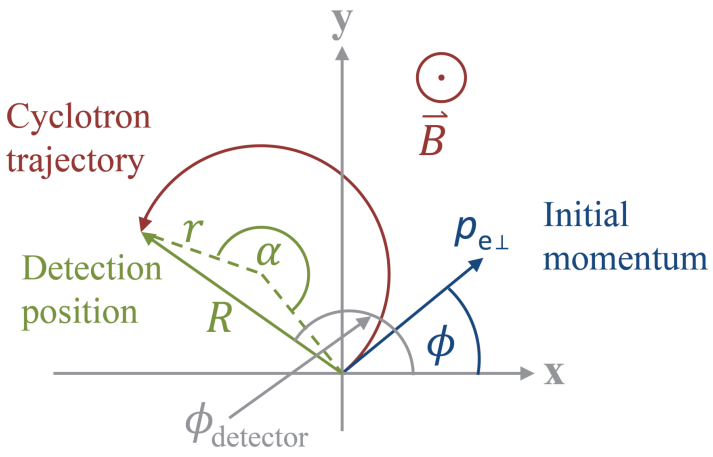

(b) Electron cyclotron motion projected in the xy-plane. Figure taken from [46]

Figure 6.7

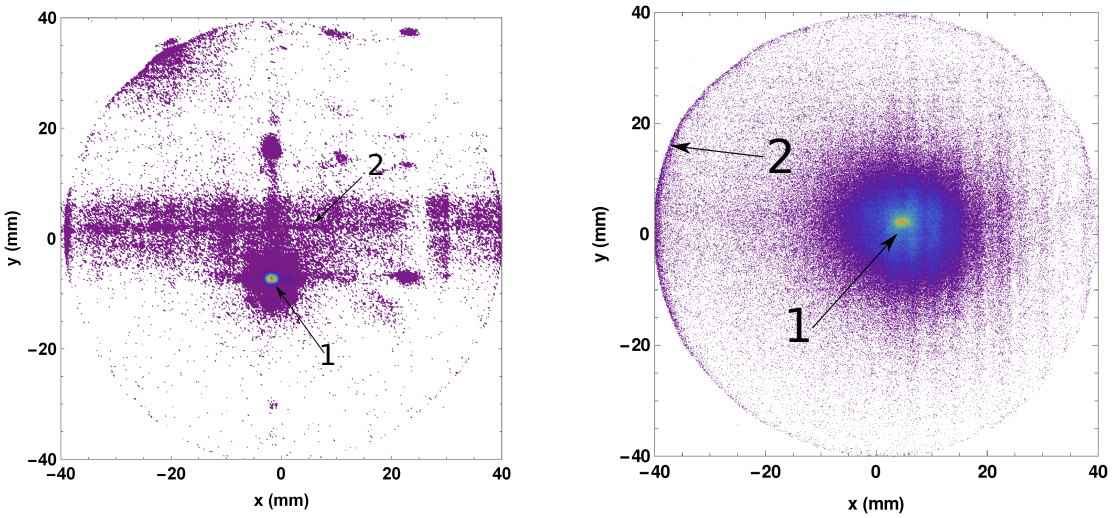

(a) Detected ions. Two regions are marked 1) ions hitting the detector below the center due to the initial velocity in the gas jet 2) ion from the rest gas in the ReMi.

(b) Detected electrons: 1)Electrons detected from ionization with the laser. 2) Electrons which are mostly noise.

Figure 6.8: Ion and Electron detectors.

equation of motion and the Lorentz force:

$$m \cdot \frac{d^2\vec{r}}{dt^2} = q \cdot (\vec{E} + \vec{v} \times \vec{B}), \tag{6.2}$$

Neglecting the effect of the magnetic field on ions, one can write the equation for the longitudinal momentum of ions:

$$L = \frac{1}{2}\, a\, TOF_{ion}^2 + v_{\parallel ion} TOF_{ion} \quad \text{with} \quad a = \frac{q}{m}\frac{U}{L}, \tag{6.3}$$

$$p_{\parallel ion} = -\frac{1}{2}\, q\, U \frac{TOF_{ion}}{L} + m\frac{L}{TOF_{ion}}, \tag{6.4}$$

where L is the acceleration length, $v_{\parallel ion}$ is the ion longitudinal velocity, m is the ion mass, q is the ion charge, and U is the acceleration voltage. To calculate the transverse momentum, the hit position on the detector has to be taken into account. Again neglecting the magnetic field effect,

$$v_{\perp ion} = \frac{r_{ion}}{TOF_{ion}} \quad with \quad r_{ion} = \sqrt{(x_{ion} - x_0)^2 + (y_{ion} - y_0)^2}, \tag{6.5}$$

where x_0 and y_0 are the transverse ionization position in the center of the ReMi and transverse momentum can be written:

$$p_{\perp ion} = \frac{r_{ion} m}{TOF_{ion}}. \tag{6.6}$$

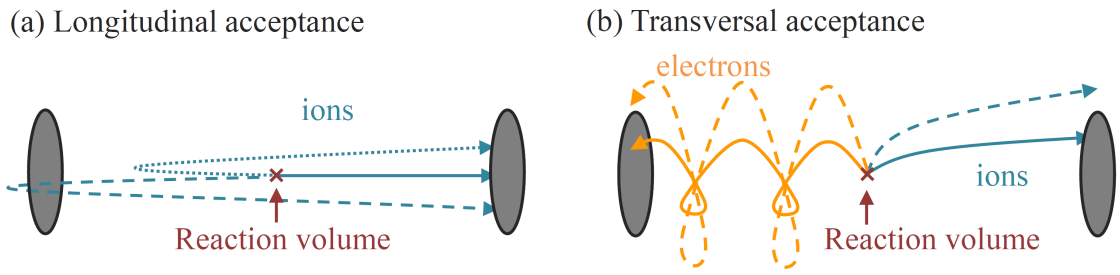

Figure 6.9: Acceptance for ions and electrons. Figure taken from [46]

Solving for x and y

$$p_{xion} = \frac{(x_{ion} - x_0)m}{TOF_{ion}}, and \quad p_{yion} = \frac{(y_{ion} - y_0)m}{TOF_{ion}}, \tag{6.7}$$

As far as electrons are concerned, because of their small charge-to-mass ratio they are traveling in helical trajectories in the magnetic field. Using equation 6.2, both the longitudinal and transverse momenta can be calculated. As for the longitudinal momentum, the same equation as 6.4 can be used. Transverse momentum, on the other hand, depends highly on the magnetic field.

$$\frac{m\ v_{\perp e}^2}{r} = e\ v_{\perp e}\ B. \tag{6.8}$$

$$p_{\perp e} = e\ r\ B. \tag{6.9}$$

The radius of the spiral motion (r) of the electrons can be determined using the position R on the detectors and the time of flight as illustrated in figure 6.7 b)

$$R = 2\ r\ |\sin\left(\frac{\alpha}{2}\right)| \quad with \quad \alpha = \omega_c \times TOF, \tag{6.10}$$

where ω_c is the cyclotron frequency. The azimuthal emission angle is then given by

$$\phi = \phi_{detector} - \frac{1}{2}\omega_c \times TOF. \tag{6.11}$$

Due to the cyclotron motion in the magnetic field, according to equation 5.11, the information about the transverse momentum is lost when $\omega_c \times TOF = 2n\pi$ which means that the electron hits the detector at position $R = 0$ as shown in figure 6.7a). Therefore the electric and magnetic fields are chosen so that electrons of interest do not fall into this region.

6.3 Acceptance

The acceptance of the reaction microscope for different particles is determined by the magnitude of the electric and magnetic fields as well as the energy of the charged particles. In the longitudinal direction as shown in figure 6.9a) , the highest detectable

energy of particles flying away from the detector is

$$E_{\parallel} = q\ U, \tag{6.12}$$

On the transverse plane as illustrated in figure 6.9b), the maximum energy for ions is given by

$$E_{\perp} = \frac{q\ U\ R_{detector}^2}{4L^2} \tag{6.13}$$

For electrons the maximum transverse energy is

$$E_{\perp} = \frac{(q\ B\ R_{detector})^2}{8m_e}. \tag{6.14}$$

Note that the magnitude of the electric and magnetic field can be increased to achieve 100 percent acceptance but this happens at the expense of the momentum resolution. The magnitude of the fields is chosen so that the maximum momentum resolution and detection of the desirable particles are guaranteed.

7 XUV Pump IR Probe in Argon and Krypton

This chapter presents the results of several XUV-IR pump-probe experiments on argon and krypton. The major goal is to observe a time modulation in photon-electron momenta resulting from double-ionization of atoms. Since time is not an observable in quantum mechanics, one has to introduce a time reference during the ionization. To achieve this goal, the XUV and IR pulses are temporally and specially overlapped in the ReMi. Then the RABITT technique is used to deduce temporal information of the system under study which provides us with a time reference which can be used to study temporal changes of the electronic wave-packet in double-ionization. Besides, Momentum resolution for different voltages of the ReMi is estimated. Finally, the 2- and 3-particle coincidences are addressed in the case of double ionization of argon and krypton.

7.1 Photo-ionization with APT

As atoms are ionized with an Attosecond Pulse Train (APT) photons, the photo-electron spectrum shows a similar pattern as the APT as illustrated in figure 7.1. The photo-electron energy is shifted by -IP (ionization potential) of the target in the ReMi, and the intensity of peaks in the photo-electron spectrum is different from that of the APT due to the difference in the cross-section of the single-photo-ionization of the target[1].

In order to doubly ionize the gas target with only one photon, higher-order harmonics are needed. As shown with a vertical dashed line in figure 7.1, the first ionization threshold of double-ionization of argon is 43.36 eV (15.7+27.6 eV) and 38.36 (14+24.36 eV) eV for krypton [55] corresponding to the 29th and 25th harmonics respectively which are much weaker in intensity compared to lower-order harmonics . This could be one of the reasons why the ratio of double- to single-ionization is very small in our case, i.e. 0.2 % for argon and 1 % for krypton. Photo-electrons resulting from single-ionization show a dipole distribution as illustrated in figure 7.2 where each half-ring in these plots belongs to photo-electrons ionized with an harmonic of the APT.

[1] The APT spectrum can be reconstructed by adding the IP to the photo-electron spectrum and dividing the spectrum by the photo-ionization cross-section given in figure 7.3 for both argon and krypton

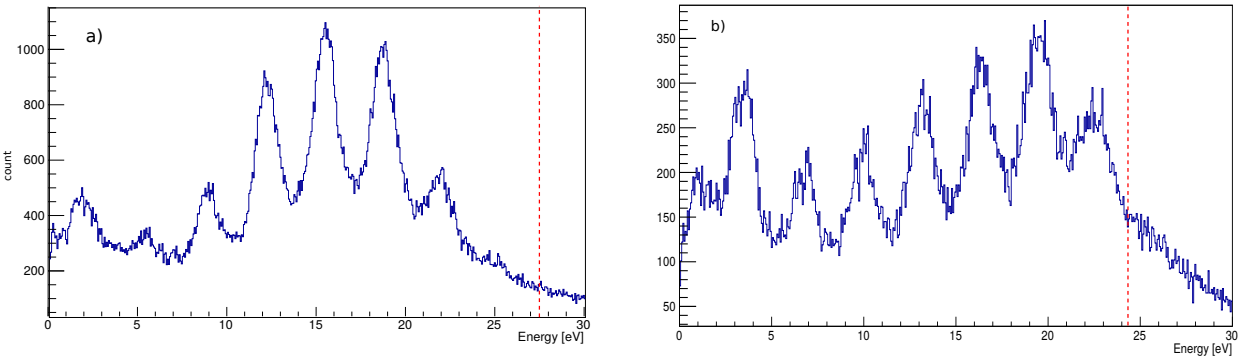

Figure 7.1: Photoelectron spectrum from the APT. Peaks are distanced by $2\hbar\omega$ where ω is the angular frequency of the driving laser field. a)Argon as gas target b) krypton as gas target

7.2 Photo-ionization in the Presence of an IR Field

In the spatial and temporal overlap of pump and probe pulses [2] , electrons after being ionized by XUV can absorb or emit, depending on the IR intensity, one or several photons , which results in the formation of side-bands. If the delay between two pulses varies, these side-bands oscillate with the frequency 2ω (T$\approx$ 1.3 fs) where ω is the frequency of the laser field. These side-bands can be used then to correct for the drift in the interferometric arms as well as finding the chirp of the APT . The matter of the utmost importance in any time-resolved experiment is the delay precision between the two interferometric arms introduced by a delay stage. In our set-up, the delay stage shows a considerable drift over time. One can, however, correct for this drift by using the peak position of one of the side-bands. In order to do so, the size of the stored data during the experiment is adjusted so that there is enough counts to see at least one side-band which is obviously oscillating which takes around 20 minutes. Then, the peak of the side-band in the first file is taken as the reference and the delay of each file of the rest of the data set is shifted so that the position of the side-band peak stays the same. In figure 7.4 the drift of the delay stage, which is the side-band peak drift over time, is illustrated for one of our longest experiment, which took nearly a weak, on argon where the position of the 22nd side-band was chosen as the reference.

7.3 Phase of XUV

After the correction for the delay stage drift, the phase of the XUV can be calculated using the RABITT method as explained in chapter 3. In order to do so , the oscillation of each side-band is investigated as shown in figure 7.5. A cosine fit

[2] To find the overlap refer to [44]p.75-6.

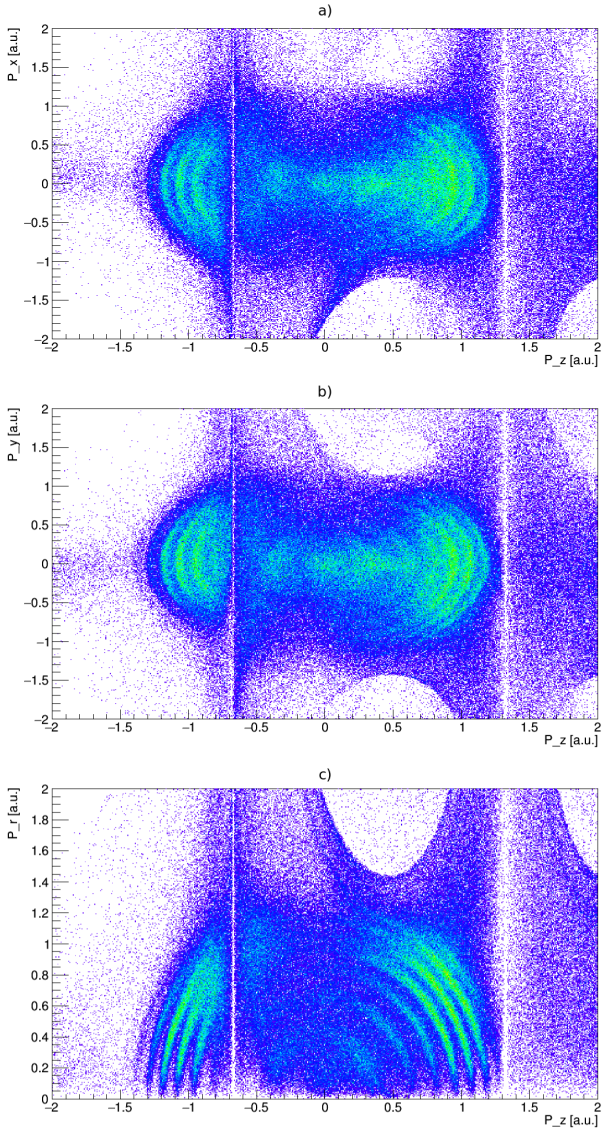

Figure 7.2: Momentum distribution of photo-electrons. The polarization vector of the XUV is along the z axis. Two parallel vertical lines in each plot show the nodes of the electron helical trajectory as a result of the magnetic field.

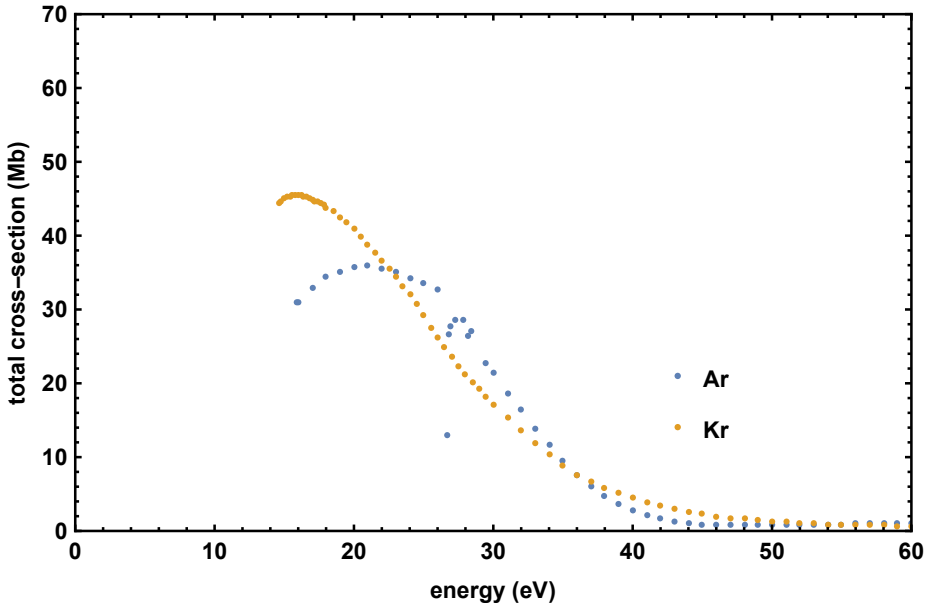

Figure 7.3: photo-ionization cross-section of argon and krypton [54].

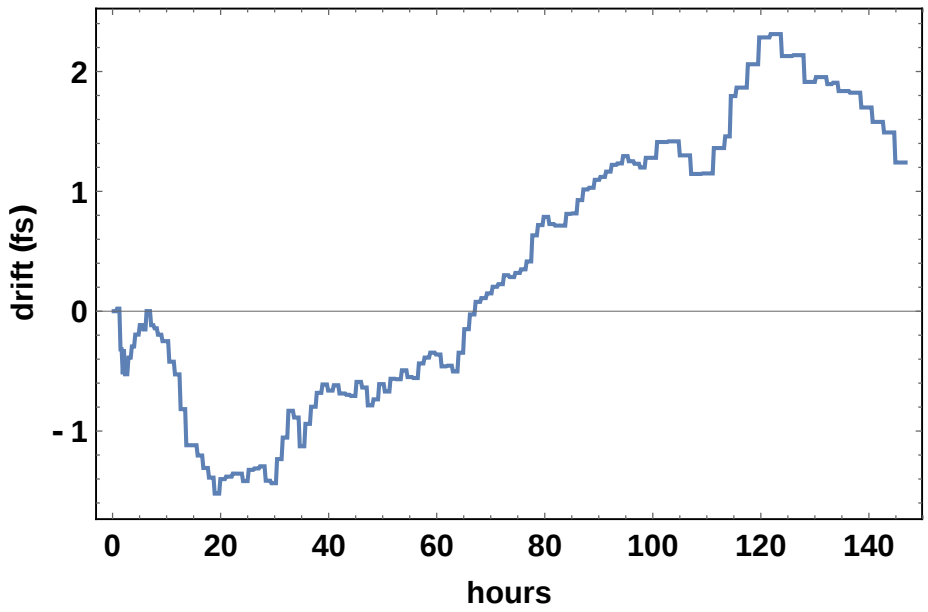

Figure 7.4: In order to assure the stability of the RABITT one interferometric arm as well as the phase of a one particular side-band can be observed. In reality with a long measurement of a couple of days, because of thermal fluctuations, there is a drift in the delay stage which can be accounted for.

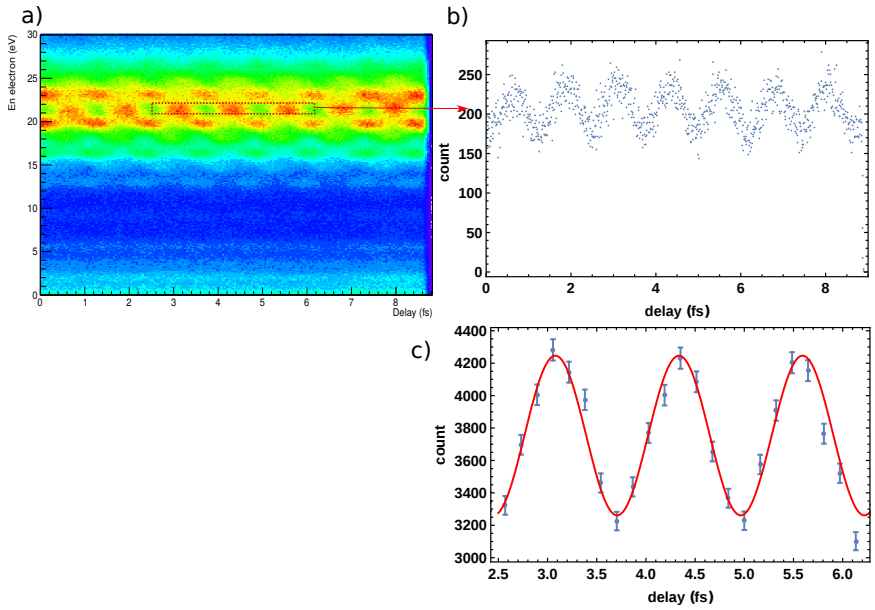

Figure 7.5: a) and b) A side-band is selected and projected onto the x axis. c) The fit function $\cos\big(2\omega(\tau+\tau_0)\big)$ is applied to the counts.

function of the form

$$\cos\big(2\omega(\tau+\tau_0)\big), \tag{7.1}$$

is applied where ω is the frequency of the laser field, τ is the delay between the APT and IR, and τ_0 is the side-band shift which, according to equation 4.12, is the sum of the XUV group delay (τ_{XUV}) and the electron wave packet (τ_W). Since τ_W is much smaller than τ_{XUV} we always approximate the group delay with τ_{XUV}. Then the phase-shift of two adjacent harmonics, according to equation 4.13, is $2\omega\tau_0$.
The frequency of the cosine function (ω) is determined using the same method but for XUV peaks because we have more counts for these peaks. The frequency ω is then determined by taking the average of the all the oscillating APT peaks. For two instances presented here, the laser wavelength in the argon case was estimated to be $755\ nm \pm 15.2\ nm$, and for krypton $762\ nm \pm 10.6\ nm$. In the next step, the same fit function with ω fixed is used to fit each side-band oscillation as illustrated in figure 7.5c). This procedure is repeated for the noticeable side-bands in the photo-electron spectrum as shown in figure 7.6a). Afterwards, the lowest side-band (18th for argon and 22nd for krypton) is taken as the reference such that its shift is zero as shown in 7.7a). Then a linear function is fitted to these points (figure 7.7) which gives the group delay of the APT (GD) $\frac{\partial\phi}{\partial\omega} \approx \frac{\Delta\phi_q}{2\omega}$ estimated to be $64\ as \pm 4.23$ and $37\ as \pm 2.78$ for argon and krypton experiments respectively. In the experiments on argon the pressure was 50mb in the HHG target and 65mb in the gas filter and the thickness of the aluminum filter was 200 nm. As for krypton, the pressure was 75 mb in the HHG target and 40 mb in the gas filter and the thickness of the aluminum filter was 200 nm.

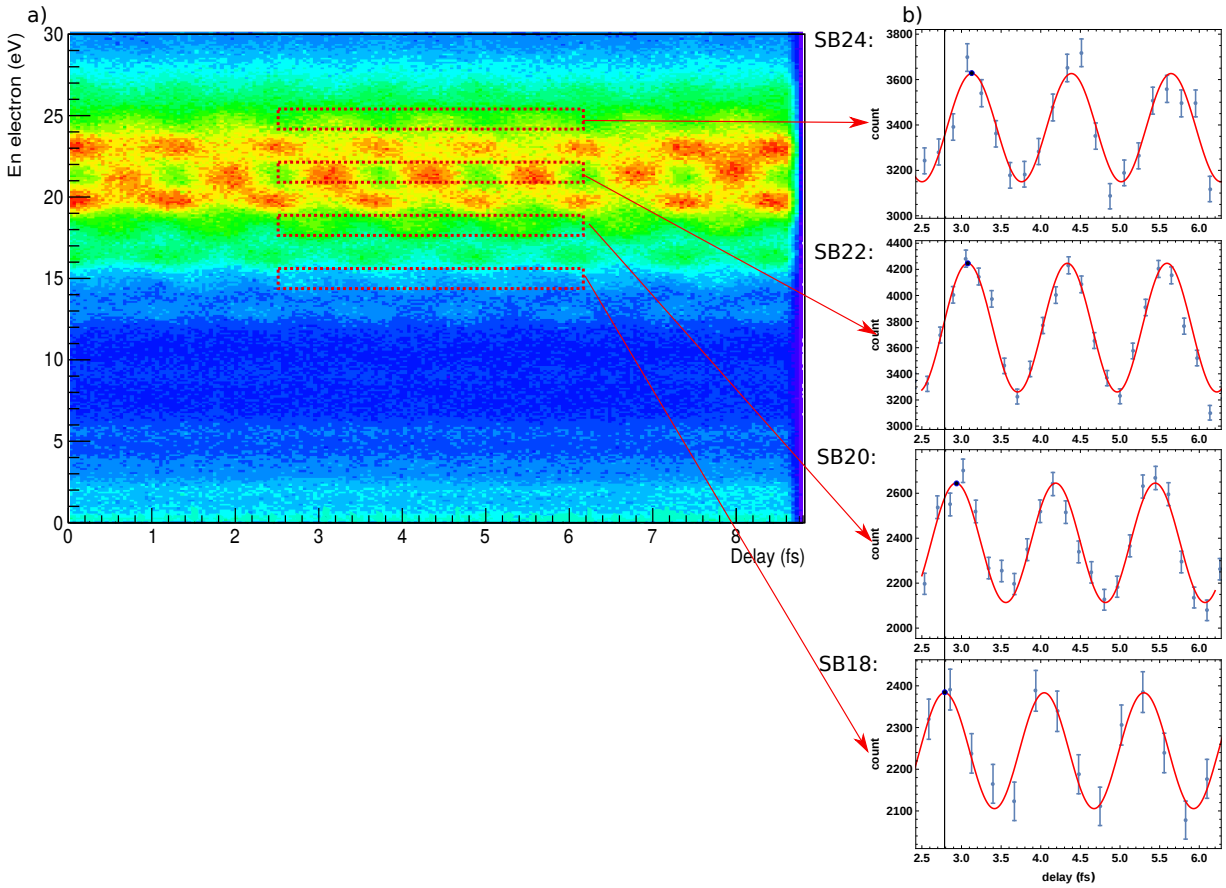

Figure 7.6: Argon ionization with the APT in the field of a weak IR. a) The photo-electron spectrum as a function of delay is shown. Side-band oscillation is repeating itself with a period of 1.3 fs. A region between 2.6 to 6.2 fs is chosen for data analysis because the amplitude of side-bands is constant. b) For each side-band a cosine function is fitted and the position of the first peak (marked with a solid point) is compared with other side-bands. A vertical line from the peak of the 18 side-band line shows the relative shift of them.

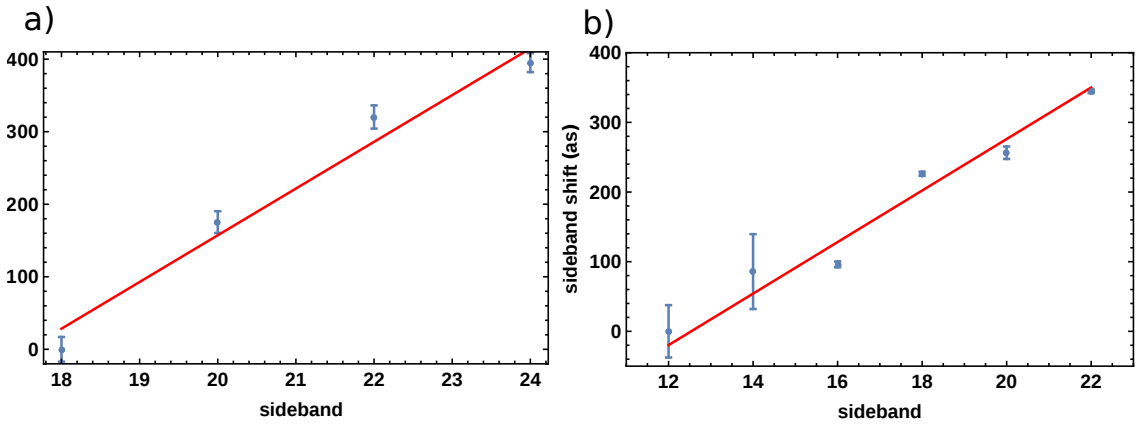

Figure 7.7: a) The side-band shift in argon is plotted and a linear function is fitted . b) The same process is repeated for krypton.

7.4 Coincidence measurement

One of the strengths of the ReMi is the possibility to do coincidence measurement to detect two, three, or more fragments simultaneously which originate from the same atom or molecule. This section shows the principle of coincidence measurements. Firstly, it is used to calculated the momentum resolution of the ReMi. Consequently, electron-ion and electron1-ion-electron2 coincidences are used to investigate the kinematics and dynamics of the double-ionization. For instance, in single-photon single-ionization, one observes a strong correlation between the recoil ion and the electron along the polarization axis as illustrated in figure 7.8 in the Ar^+-e coincidence where an Ar^+ and electron are detected in coincidence. The diagonal line shows the momentum conservation in single ionization of argon where

$$p_z ion + p_z electron = 0. \tag{7.2}$$

One can then exclude any counts but the diagonal line as false coincidences by applying a conditions around this region. The origin of these false coincidences could be the acquisition fault which happens when the ionization rate exceeds the repetition rate of the laser. Therefore, during a laser pulse, ionization events which do not belong to the same target could be detected in coincidence, and some ionization resulting from scattered XUV hitting plates, rims, in the ReMi.

7.4.1 Momentum Resolution

The momentum resolution is determined mostly by the ion momentum resolution because of the relatively high precision of the electron momentum detection. The limiting factors in the resolution are the momentum spread in the gas jet and the spectrometer resolution. For complete calculations of the momentum of the gas and the spectrometer uncertainty refer to [44]. Since measuring the momentum resolution of individual particles is a difficult task in an experiment, it is generally defined

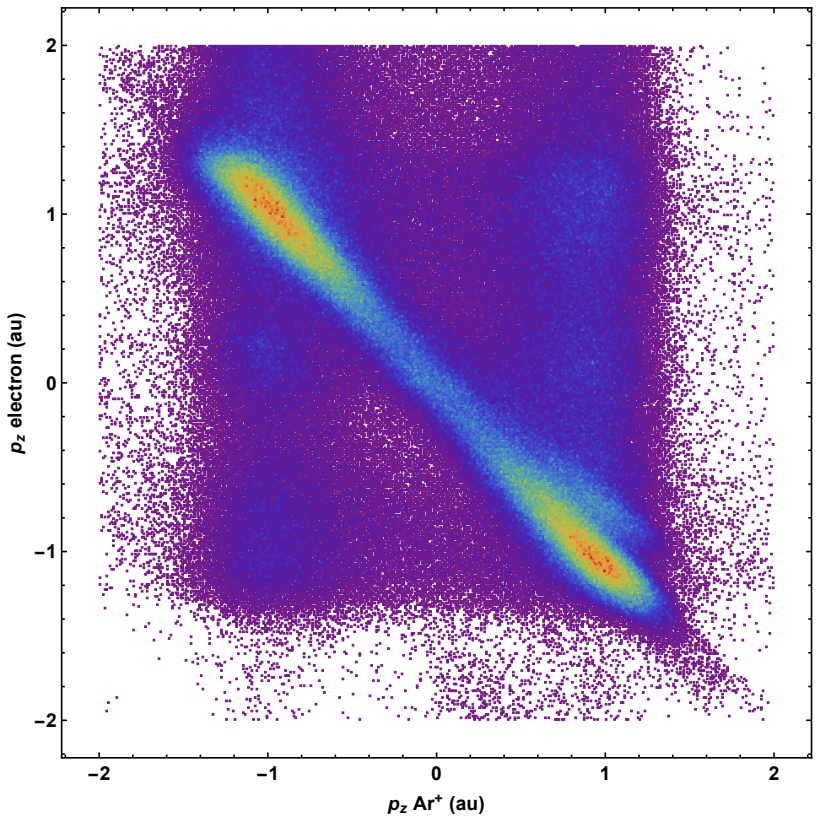

Figure 7.8: The longitudinal momentum distribution of the single-ionization of argon with one photon in the Ar^+-e coincidence. The horizontal axis shows the recoil ion momentum and the vertical one shows that of the electron. Since the incoming photon momentum can be neglected the ion-electron pair is emitted back-back with the same momentum which manifests itself as a diagonal line in this momentum correlation plot. The width of the diagonal line is the momentum resolution. Any other events are considered as false coincidences.

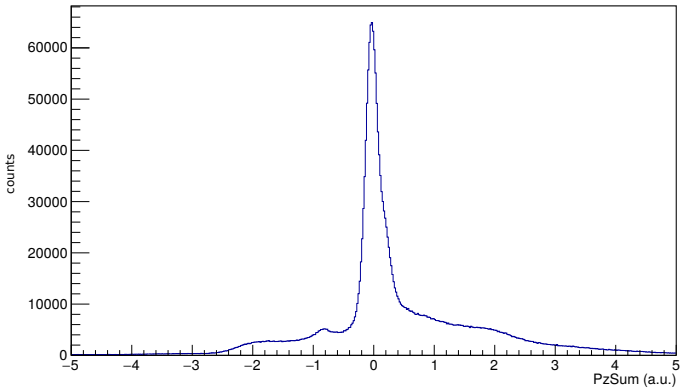

Figure 7.9: p_z sum of Ar^+ and e in coincidence measurement where Ar^+-e pairs were detected in coincidence. The FWHM of the central peak is generally assumed to be the momentum resolution.

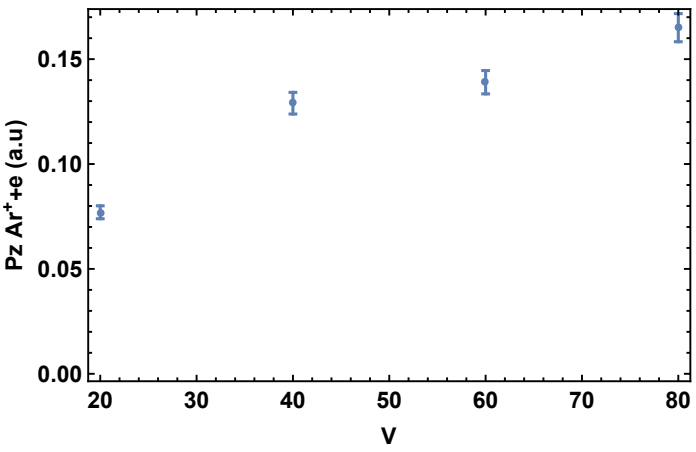

Figure 7.10: Longitudinal momentum (p_z) sum of Ar^+ and e for different voltages of the spectrometer.

using the momentum sum of electrons and ions which are detected in coincidence. In figure 7.9 the longitudinal momentum sum of electrons and Ar^+ is shown whose FWHM defines the momentum resolution. In this case, the resolution is measured to be 0.18 $au \pm 0.01$ au with an extraction voltage of 90 V and magnetic field of 8 Gauss. The broad wings of the plot correspond to the ion-electron pairs which do not belong to this coincidence or as they are often called false coincidences. As explained in chapter 6, the momentum resolution in theory is inversely proportional to the extraction voltage. The momentum resolution of argon for different voltages is given in figure 7.10 where the resolution increases with lowering the voltage.

7.5 Momentum Correlation in Single-photon Double-Ionization of Argon and Krypton

In this final section, the electron-electron correlation is investigated for the mechanism of double ionization. The main interest lies in the fact that how the photon excess energy after ionization can be distributed between the electrons. This means that we need to record the properties of two particles simultaneously. Technically, this is fulfilled by doing coincidence measurement where the electrons recorded in coincidence with an ion^++ are analyzed. Two schemes are possible: ion^{++}-e and e-ion^{++}-e coincidences as explained in the following.

Electron-Ion^{++}-Electron coincidence

In the e-ion^{++}-e coincidence, one doubly-charged ion is detected in coincidence with two electrons. To confirm if these electrons belong to the double-ionization, one can use the momentum conservation:

$$p_z ion^{++} = -(p_z electron\ 1 + p_z electron\ 2). \tag{7.3}$$

In figure 7.11 the above equation is plotted in the case of krypton for two different extraction voltages. The plot ($p_z Kr^{++}$ vs. (p_z electron 1 + p_z electron 2)) has to have ideally only a diagonal line. As shown in the first row of figure 7.11, there are some electrons (indicated by red arrows) which are not on the diagonal line, and thus these are ruled out as false coincidences. Moreover, when the extraction voltage is higher many more electrons are falsely attributed to this coincidence which appear anywhere but on the diagonal line, whereas, with a lower voltage this noise is considerably reduced as shown in the right panel. This is more obvious if the p_z sum of all the three particles (ion, electron 1, and electron 2) are plotted as illustrated in the second row of figure 7.11. Afterwards, the longitudinal momentum of the the two detected electrons are plotted as shown in figure 7.12. The important characteristic is the empty diagonal space in the middle which happens as a result of the detectors dead-time which means that the detector can not detect two particles exactly simultaneously. In fact there is around 10ns time needed for detectors to

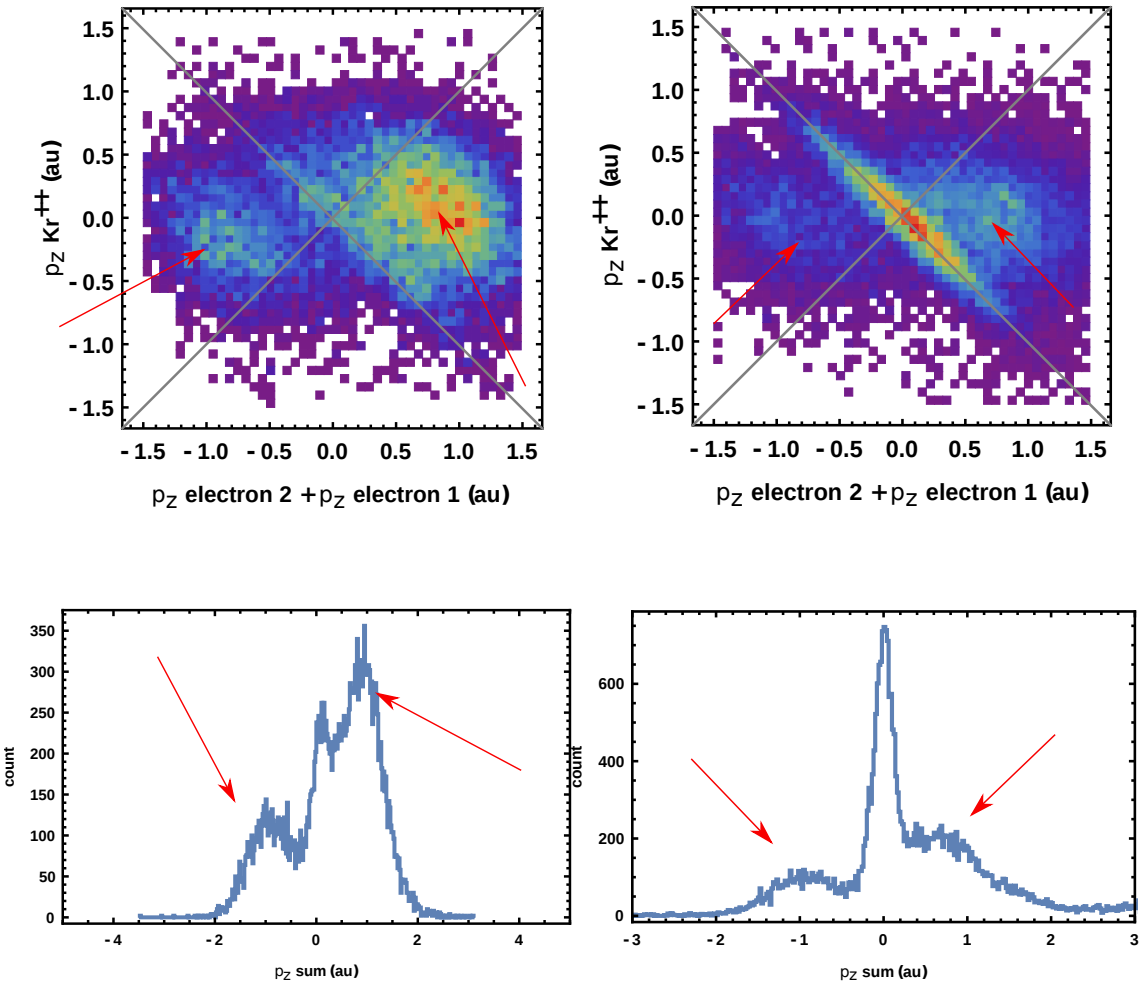

(a) Extraction voltage 90 V.

(b) Extraction voltage 20 V

Figure 7.11: In the first row the p_z sum of two electrons vs p_z of Kr^{++} is plotted where only counts on the diagonal line corresponding to $p_z Kr^{++} = -(p_z$ electron 1 + p_z electron 2) are the true ones. A strong background is obvious in the left plot due to the high extraction voltage which cause many electrons to be detected as false coincidences as marked with red arrows. In the second row, the p_z sum of Kr^{++}, electron 1 and electron 2 is plotted. Only the peak centered at zero momentum corresponds to true coincidences. Diagonal gray lines are guides to the eye.

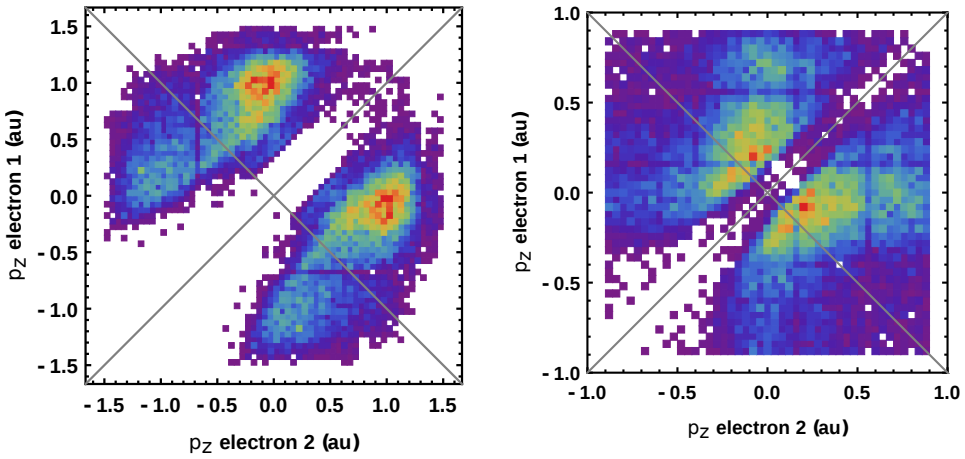

Figure 7.12: The longitudinal momentum of the two detected electrons in e-Kr^{++}-e coincidence is plotted, left for 90 V and right for 20 V. Diagonal empty region is the detector dead region which is bigger for the higher voltage. Diagonal gray lines are guides to the eye.

be able to detect another particle after the first detection. As shown in the figure the smaller extraction voltage can considerably reduce the dead-time zone as the electron distribution is spread in time.

Ion^{++}-Electron coincidence

In the ion^{++}-e coincidence, two charged particles (Ion^{++} and e) of three-particle double ionization are detected in coincidence and the momentum of the third not-detected electron can be reconstructed by means of the momentum conservation because the momentum of the incoming photon is neglected. The resulting momentum distribution of krypton with a extraction voltage of 20 V is illustrated in figure 7.13. The horizontal axis shows the longitudinal momentum of the reconstructed electron and the vertical axis the detected one.

Electron-Electron Correlation

Two electrons are said to be correlated when the probability of simultaneously finding electron 1 is dependent on finding electron 2. In order to investigate this phenomenon, one can first produce a correlated plot where, according to figure 7.14a), the longitudinal momentum of two electrons from each event is plotted against each other. Then by producing an uncorrelated plot where the longitudinal momentum is randomly plotted against any other electron as shown in figure 7.14b). By comparing these two cases one can see if there is any change in the structure of the momentum distribution. The example of krypton is considered here. As illustrated in figure 7.15, for both coincidences the correlated and uncorrelated plots are compared. Diagonal gray and vertical red lines are guides to the eye. As one can see, the structure in both cases remains almost the same. The same procedure was repeated

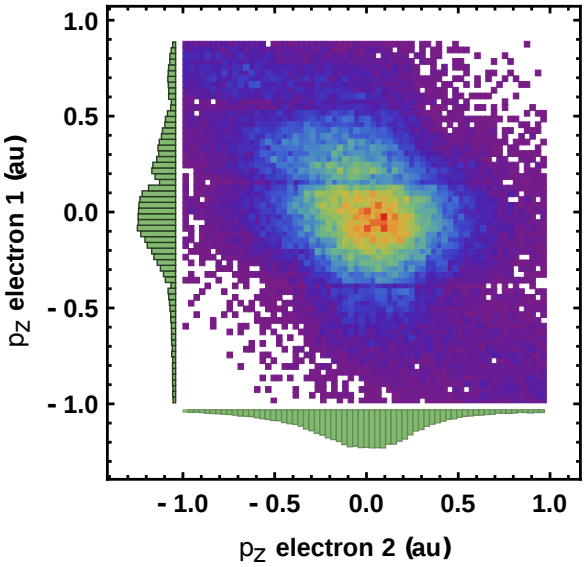

Figure 7.13: Longitudinal momentum (p_z) of two electrons In the Kr^{++}-e coincidence where the momentum of electron 2 is reconstructed .

a)

event		
1	P_z electron 1 ↔	P_z electron 1
2	P_z electron 1 ↔	P_z electron 1
3	P_z electron 1 ↔	P_z electron 1
.	.	.
.	.	.
.	.	.

b)

event		
1	P_z electron 1	P_z electron 1
2	P_z electron 1	P_z electron 1
3	P_z electron 1	P_z electron 1
.	.	.
.	.	.
.	.	.

Figure 7.14: a) The longitudinal momentum of electron 1 and 2 in each correlated event. b) The longitudinal momentum of electron 1 of one event is related to the that of electron 2 from any other event to create uncorrelated events.

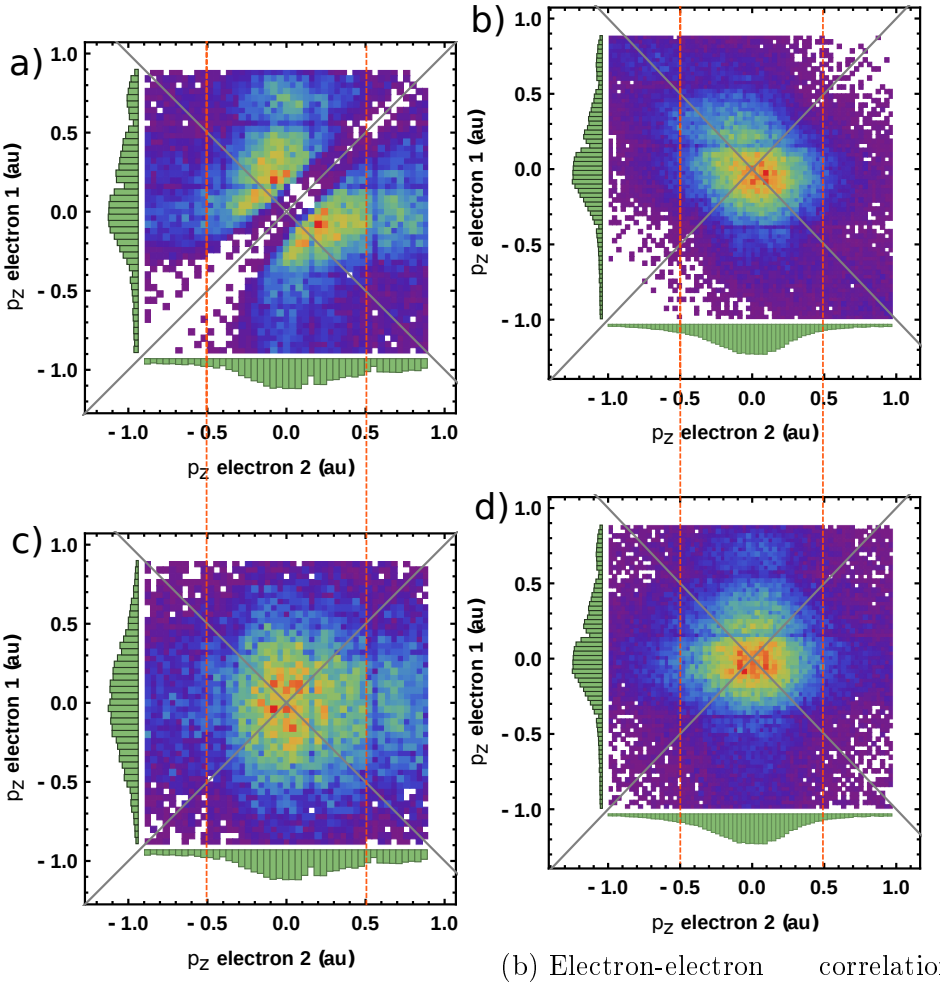

(a) Electron-electron correlation in e-Kr^{++}-e coincidence, where the momentum of the two detected electrons are plotted. c) The momentum of one of electron 2 is randomized to create an uncorrelated momentum distribution. Cross gray and vertical red lines are guides to the eye.

(b) Electron-electron correlation in $Kr^{+} - e$ coincidence where the p_z momentum of the not-detected electron is reconstructed first and plotted against the detected one. d) The momentum of one of the electrons is randomized to create an uncorrelated plot. Cross gray and vertical red lines are guides to the eye

Figure 7.15

for various measurements on both argon and krypton. No strong correlation was observed maybe due to the resolution in the case of the 2 particle coincidence and the noise in the 3-particle one.

Finally, the longitudinal momentum of different particles from different coincidences is plotted as a function of time. As illustrated in figure 7.16. Unfortunately, there is no time-dependent structure to be observed probably due to the lack of statistics.

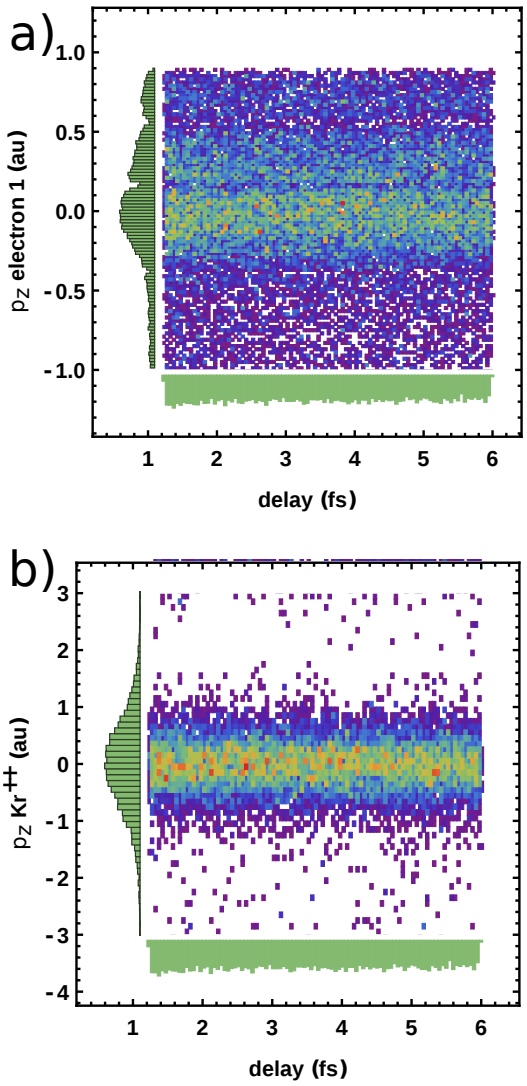

Figure 7.16: The longitudinal momentum of the electron 1 and Kr^{++} as a function of the delay between XUV and IR pulse in e-Kr^{++}-e coincidence. No modulation can be seen in any of these plots

8 Summary and Outlook

This thesis presents the results of several pump-probe experiments on argon and krypton. An HHG source is used to produce an attosecond pulse train (APT) as a pump pulse to ionize the target and an IR pulse is delayed relative to the pump. The resulting so-called spectrogram is then plotted as a function of the delay. The sideband oscillation is used to correct for the drift of the delay stage and also to investigate the chirp of the APT using the RABITT method. Then, different coincidences in the ReMi are used to study the correlated momenta of the emitted two electrons in the presence of a weak IR field so as to have a time reference according to which the dynamics of the double-ionization of argon and krypton could be studied. Unfortunately no time-dependency in the photoelectron momenta has been observed. The reason for this could be that the number of double-ionization events is not enough. There are, however, ways to increase this number.

In order to improve the ratio of double- to single-ionization, a pair of wedges is being installed after the hollow-core fiber so that its combination with the chirped mirrors could provide a shorter pulse duration, thus creating more high energetic photons during HHG. In our case, the pulse duration is around 22 fs second. In fact, with long pulses the medium where HHG takes place could be depleted even before the peak of the pulse, which reduces the intensity of high-energetic harmonic peaks. That means if the pulse gets shorter the ratio of high- to low-energetic photons increases which ultimately improves the double- to single-photoionization ratio. Very recently by putting some glass substrates after the hollow-core fiber the quality of the plasma in the HHG metal tube was improved, and as a result the ratio has increased considerably. It is estimated that with our laser system the double- to single-ionization ratio could be increased to 1 % for argon and 10 % for krypton at a single-ionization rate of around 1000 count/s.

Another option would be to decrease the extraction voltage and the magnetic field even further in order to make the detector dead time smaller because electrons will be spread more in time. Reducing the electric and magnetic field is also beneficial because many high-energetic photoelectrons, resulting from the single-ionization, which normally appear as noise, would not be detected. As a result, the ratio of the detected high-energetic photoelectrons (mostly belong to the single-ionization) to low-energetic photoelectrons (among which many result from double-ionization) decreases.

On the data analysis side, with much higher double-ionization events, one can focus on even angle-resolved analysis of the photoelectron spectrum resulting from double-ionization in our ReMi to make the most of its potential.

9 Atomic Units

In order to simplify the calculations and expressions in atomic physics, one can set all the constants in the electronic Schrödinger Equation equal to one atomic unit.

$$\hbar = m_e = e = 4\pi\epsilon_0 = 1a.u \tag{9.1}$$

The atomic units correspond to the electron in the ground state of the Hydrogen atom. Other quantities can be calculated with the above definition:

Quantity	Definition	SI Value
Mass	m_e	$9.1093897 \times 10^{-31}$kg
Charge	e	$1.6021773 \times 10^{-19}$C
Length	Bohr Radius a_0	$5.29177249 \times 10^{-11}$m
Angular Momentum	$\hbar$	$1.0545887 \times 10^{-34}$Js
Velocity	αc	2.18769142×10^{8}m/s
Energy	$m_e(\alpha c)^2$	44.3593×10^{-34} J
Time	$a_0(\alpha c)^{-1}$	$2.41888433 \times 10^{-17}$s

List of Figures

Bibliography

[1] R. Dörner, Th. Weber, M. Weckenbrock, A. Staudte, M. Hattass, H. Schmidt-Böcking, R. Moshammer, and J. Ullrich. Multiple ionization in strong laser fields. volume 48 of *Advances In Atomic, Molecular, and Optical Physics*, pages 1 – 34. Academic Press, 2002.

[2] M Schulz, D Fischer, R Moshammer, and J Ullrich. Electron–electron correlations and dipole selection rules in double ionization of helium by proton impact. *Journal of Physics B: Atomic, Molecular and Optical Physics*, 38(8):1363, 2005.

[3] Ferenc Krausz and Misha Ivanov. Attosecond physics. *Rev. Mod. Phys.*, 81:163–234, Feb 2009.

[4] Uwe Morgner. *Ultrafast Laser Oscillators and Amplifiers*, pages 17–36. 2014.

[5] D.J. Griffiths. *Introduction to Electrodynamics*. Prentice Hall, 1999.

[6] File:gaussianbeamwaist.svg.

[7] Paul Adrien Maurice Dirac. *Modern Optics 2ed Edition*. Oxford University Press, 2015.

[8] Hermite-gaussian.

[9] Eli Yablonovitch. Inhibited spontaneous emission in solid-state physics and electronics. *Phys. Rev. Lett.*, 58:2059–2062, May 1987.

[10] V. Berger. Nonlinear photonic crystals. *Phys. Rev. Lett.*, 81:4136–4139, Nov 1998.

[11] C. Rulliere. *Femtosecond Laser Pulses: Principles and Experiments*. Advanced Texts in Physics. Springer, 2005.

[12] Donna Strickland and Gerard Mourou. Compression of amplified chirped optical pulses. *Optics Communications*, 56(3):219 – 221, 1985.

[13] M. Nisoli, S. De Silvestri, and O. Svelto. Generation of high-energy 10-fs pulses by a new pulse compression technique. In *Conference on Lasers and Electro-Optics*, page CTuR5. Optical Society of America, 1996.

[14] M. Kolesik, E. M. Wright, J. Andreasen, J. M. Brown, D. R. Carlson, and R. J. Jones. Space-time resolved simulation of femtosecond nonlinear light-matter interactions using a holistic quantum atomic model : Application to near-threshold harmonics. *Opt. Express*, 20(14):16113–16128, Jul 2012.

[15] P. A. Franken, A. E. Hill, C. W. Peters, and G. Weinreich. Generation of optical harmonics. *Phys. Rev. Lett.*, 7:118–119, Aug 1961.

[16] A. McPherson, G. Gibson, H. Jara, U. Johann, T. S. Luk, I. A. McIntyre, K. Boyer, and C. K. Rhodes. Studies of multiphoton production of vacuum-ultraviolet radiation in the rare gases. *J. Opt. Soc. Am. B*, 4(4):595–601, Apr 1987.

[17] M Ferray, A L'Huillier, X F Li, L A Lompre, G Mainfray, and C Manus. Multiple-harmonic conversion of 1064 nm radiation in rare gases. *Journal of Physics B: Atomic, Molecular and Optical Physics*, 21(3):L31, 1988.

[18] Gy. Farkas and Cs. Tóth. Proposal for attosecond light pulse generation using laser induced multiple-harmonic conversion processes in rare gases. *Physics Letters A*, 168(5–6):447 – 450, 1992.

[19] N. A. Papadogiannis, B. Witzel, C. Kalpouzos, and D. Charalambidis. Observation of attosecond light localization in higher order harmonic generation. *Phys. Rev. Lett.*, 83:4289–4292, Nov 1999.

[20] L. A. Lompré, A. L'Huillier, M. Ferray, P. Monot, G. Mainfray, and C. Manus. High-order harmonic generation in xenon: intensity and propagation effects. *J. Opt. Soc. Am. B*, 7(5):754–761, May 1990.

[21] Tenio Popmintchev, Ming-Chang Chen, Paul Arpin, Margaret M. Murnane, and Henry C. Kapteyn. The attosecond nonlinear optics of bright coherent x-ray generation. *Nat Photon*, 4(12):822–832, Dec 2010.

[22] P. B. Corkum. Plasma perspective on strong field multiphoton ionization. *Phys. Rev. Lett.*, 71:1994–1997, Sep 1993.

[23] Frank Träger, editor. *Nonlinear Optics*, pages 157–248. Springer New York, New York, NY, 2007.

[24] Christoph Heyl. *Scaling and Gating Attosecond Pulse Generation*. PhD thesis, Lund University, 2014.

[25] Esben Witting Larsen. *Attosecond Sources and Interferometers - Developments and Applications*. PhD thesis, Lund University, 2016.

[26] Kathrin Klünder. *Electron Wave Packet Dynamics on the Attosecond Time Scale*. PhD thesis, Lund University, 2012.

[27] Philippe Balcou, Pascal Sali'eres, Anne L'Huillier, and Maciej Lewenstein. Generalized phase-matching conditions for high harmonics: The role of field-gradient forces. *Phys. Rev. A*, 55:3204–3210, Apr 1997.

[28] A. L'Huillier, K. J. Schafer, and K. C. Kulander. Higher-order harmonic generation in xenon at 1064 nm: The role of phase matching. *Phys. Rev. Lett.*, 66:2200–2203, Apr 1991.

[29] Ph. Balcou and Anne L'Huillier. Phase-matching effects in strong-field harmonic generation. *Phys. Rev. A*, 47:1447–1459, Feb 1993.

[30] Thomas Remetter. *Attosecond Electron Wave Packet Interferences*. PhD thesis, Lund University, 2008.

[31] H.G. Muller. Reconstruction of attosecond harmonic beating by interference of two-photon transitions. *Applied Physics B*, 74(1):s17–s21, 2002.

[32] P. M. Paul, E. S. Toma, P. Breger, G. Mullot, F. Augé, Ph. Balcou, H. G. Muller, and P. Agostini. Observation of a train of attosecond pulses from high harmonic generation. *Science*, 292(5522):1689–1692, 2001.

[33] Anthony Starace. *Photoionization of Atoms*, pages 379–390. Springer New York, New York, NY, 2006.

[34] M. Ya. Amusia. *Photoabsorption in the One-Electron Approximation*. Springer US, Boston, MA, 1990.

[35] B H Bransden and C J Joachain. *Physics of Atoms and Molecules; 2nd ed.* Prentice-Hall, Harlow, 2003.

[36] L. Fechner. *High resolution experiments on strong-field ionization of atoms and molecules: test of tunneling theory, the role of doubly excited statesand channel-selective electron spectra*. PhD thesis, Heidelberg Univeristy, 2014.

[37] Tobias Schneider and Jan-Michael Rost. Double photoionization of two-electron atoms based on the explicit separation of dominant ionization mechanisms. *Phys. Rev. A*, 67:062704, Jun 2003.

[38] Per Linusson. *Single-photon multiple ionization processes studied by electron coincidence spectroscopy*. PhD thesis, tockholm University,, 2013.

[39] T Pattard, T Schneider, and J M Rost. On the role of shake-off in single-photon double ionization. *Journal of Physics B: Atomic, Molecular and Optical Physics*, 36(12):L189, 2003.

[40] Reinhard Dörner, Horst Schmidt-Böcking, Thorsten Weber, Till Jahnke, Markus Schöffler, Alexandra Knapp, Mirko Hattass, Achim Czasch, Lothar Ph. H. Schmidt, and Ottmar. Double ionization by one and many photons. *Radiation Physics and Chemistry*, 70(1–3):191 – 206, 2004. Photoeffect: Theory and Experiment.

[41] Eugene P. Wigner. Lower limit for the energy derivative of the scattering phase shift. *Phys. Rev.*, 98:145–147, Apr 1955.

[42] J.M. Dahlström, D. Guénot, K. Klünder, M. Gisselbrecht, J. Mauritsson, A. L'Huillier, A. Maquet, and R. Taïeb. Theory of attosecond delays in laser-assisted photoionization. *Chemical Physics*, 414:53 – 64, 2013. Attosecond spectroscopy.

[43] A. L. Cavalieri, N. Muller, Th Uphues, V. S. Yakovlev, A. Baltuska, B. Horvath, B. Schmidt, L. Blumel, R. Holzwarth, S. Hendel, M. Drescher, U. Kleineberg, P. M. Echenique, R. Kienberger, F. Krausz, and U. Heinzmann. Attosecond spectroscopy in condensed matter. *Nature*, 449(7165):1029–1032, Oct 2007.

[44] Philipp Cörlin. *Tracing ultra-fast molecular dynamics in O 2 + and N 2 + with XUV–IR pump–probe experiments.* PhD thesis, Heidelberg Univeristy, 2015.

[45] M. Nisoli, E. Priori, G. Sansone, S. Stagira, G. Cerullo, S. De Silvestri, C. Altucci, R. Bruzzese, C. de Lisio, P. Villoresi, L. Poletto, M. Pascolini, and G. Tondello. High-brightness high-order harmonic generation by truncated bessel beams in the sub-10-fs regime. *Phys. Rev. Lett.*, 88:033902, Jan 2002.

[46] Alexander Georg Sperl. *XUV-IR pump-probe experiments: Exploring nuclear and electronic correlated quantum dynamics in the hydrogen molecule.* PhD thesis, Heidelberg Univeristy, 2013.

[47] Michael Schönwald. *On the Contribution of autoionizing states to XUV radiation-induced double ionization of nitrous oxide (N 2 O).* PhD thesis, Heidelberg Univeristy, 2015.

[48] B.L. Henke, E.M. Gullikson, and J.C. Davis. X-ray interactions: Photoabsorption, scattering, transmission, and reflection at e = 50-30,000 ev, z = 1-92. *Atomic Data and Nuclear Data Tables*, 54(2):181 – 342, 1993.

[49] J Ullrich, R Moshammer, A Dorn, R Dörner, L Ph H Schmidt, and H Schmidt-Böcking. Recoil-ion and electron momentum spectroscopy: reaction-microscopes. *Reports on Progress in Physics*, 66(9):1463, 2003.

[50] Philipp Cörlin. Laser induced coulomb-explosion of allene molecules: Experiment and simulation. Master's thesis, Heidelberg University, 9 2012.

[51] R. Campargue. Progress in overexpanded supersonic jets and skimmed molecular beams in free-jet zones of silence. *The Journal of Physical Chemistry*, 88(20):4466–4474, 1984.

[52] Ram Gopal. *Electron Wave Packet Interferences in Ionization with Few-Cycle Laser Pulses and the Dissociative Photoionization of D2 with Ultrashort Extreme Ultraviolet Pulses.* PhD thesis, Heidelberg Univeristy, 2010.

[53] Martin Laux. *Construction and characterization of a new Reaction Microscope*. PhD thesis, University of Heidelberg, 2011.

[54] J.A.R. Samson and W.C. Stolte. Precision measurements of the total photoionization cross-sections of he, ne, ar, kr, and xe. *Journal of Electron Spectroscopy and Related Phenomena*, 123(2–3):265 – 276, 2002. Determination of cross-sections and momentum profiles of atoms, molecules and condensed matter.

[55] R I Hall, K Ellis, A McConkey, G Dawber, L Avaldi, M A MacDonald, and G C King. Double and single ionization of neon, argon and krypton in the threshold region studied by photoelectron-ion coincidence spectroscopy. *Journal of Physics B: Atomic, Molecular and Optical Physics*, 25(2):377, 1992.

Acknowledgement

Firstly, I would like to express my sincere gratitude to my supervisor Priv.-Doz. Dr. Robert Moshammer for his expertise, understanding, and kindness. He let me have a highly rewarding experience in his group by giving me a complete freedom, more importantly the courage to be able to independently run the Attolab.
I would like to thank specially my colleague Frans Schotsch for his feedback, cooperation, and the proofread of my thesis. Every result in this thesis was accomplished with his help and support.
I am also grateful to Dr. Nicolas Camus for his help and kindness during the course of my thesis as well as the correction of my thesis.
I would also like to acknowledge Priv.-Doz. Dr. Alexander Dorn as the second examiner of this thesis.
Besides, I would like to thank our former group members Philipp Cörlin and Andreas Fischer for their relentless effort to support me in any respect.
I would also like to take this opportunity to express my warm thanks to Prof. Dr. Thomas Pfeifer for his help, support, and insightful remarks all along the way. Finally, I would like to thank Dr. Claus Dieter Schröter and Bernd Knape for their technical support over the course of my thesis.

Erklärung:

Ich versichere, dass ich diese Arbeit selbstständig verfasst habe und keine anderen als die angegebenen Quellen und Hilfsmittel benutzt habe.

Heidelberg, den (Datum) .....